LJMU Research Online

Srinivasaragavan, GP, Hamidani, H, Schroeder, G, Sarin, N, Ho, AYQ, Piro, AL, Cenko, SB, Anand, S, Sollerman, J, Perley, DA, Maeda, K, O'Connor, B, Kuncarayakti, H, Miller, MC, Ahumada, T, Vail, JL, Duffell, P, Dastidar, R, Andreoni, I, Bochenek, A, Brennan, SJ, Carney, J, Chen, P, Freeburn, J, Gal-Yam, A, Jacobson-Galán, W, Kasliwal, MM, Li 李, J 嘉, Li, ML, Sravan, N and Warshofsky, DE

 EP250108a/SN 2025kg: A Jet-driven Stellar Explosion Interacting with Circumstellar Material

https://researchonline.ljmu.ac.uk/id/eprint/26887/

Article

For more information please contact researchonline@ljmu.ac.uk

EP250108a/SN 2025kg: A Jet-driven Stellar Explosion Interacting with Circumstellar Material

Gokul P. Srinivasaragavan[1,2,3] , Hamid Hamidani[4] , Genevieve Schroeder[5] , Nikhil Sarin[6,7] , Anna Y. Q. Ho[5] ,
Anthony L. Piro[8] , S. Bradley Cenko[2,3] , Shreya Anand[9,10] , Jesper Sollerman[11] , Daniel A. Perley[12] , Keiichi Maeda[13] ,
Brendan O'Connor[14] , Hanindyo Kuncarayakti[15,16] , M. Coleman Miller[1,2] , Tomás Ahumada[17] , Jada L. Vail[5] ,
Paul Duffell[18] , Ranadeep Dastidar[18] , Igor Andreoni[19] , Aleksandra Bochenek[12] , Seán. J. Brennan[20] ,
Jonathan Carney[19] , Ping Chen[21] , James Freeburn[22,23] , Avishay Gal-Yam[21] , Wynn Jacobson-Galán[17] ,
Mansi M. Kasliwal[17] , Jiaxuan Li (李嘉轩)[24] , Maggie L. Li[17] , Niharika Sravan[25] , and Daniel E. Warshofsky[26]

[1] Department of Astronomy, University of Maryland, College Park, MD 20742, USA; gsriniv2@umd.edu
[2] Joint Space-Science Institute, University of Maryland, College Park, MD 20742, USA
[3] Astrophysics Science Division, NASA Goddard Space Flight Center, 8800 Greenbelt Rd., Greenbelt, MD 20771, USA
[4] Astronomical Institute, Graduate School of Science, Tohoku University, Sendai 980-8578, Japan
[5] Department of Astronomy, Cornell University, Ithaca, NY 14853, USA
[6] Oskar Klein Centre for Cosmoparticle Physics, Department of Physics, Stockholm University, AlbaNova, Stockholm SE-106 91, Sweden
[7] Nordita, Stockholm University and KTH Royal Institute of Technology, Hannes Alfvéns väg 12, SE-106 91 Stockholm, Sweden
[8] The Observatories of the Carnegie Institution for Science, 813 Santa Barbara St., Pasadena, CA 91101, USA
[9] Kavli Institute for Particle Astrophysics and Cosmology, Stanford University, 452 Lomita Mall, Stanford, CA 94305, USA
[10] Department of Astronomy, University of California, Berkeley, CA 94720-3411, USA
[11] Department of Astronomy, The Oskar Klein Center, Stockholm University, AlbaNova, 10691 Stockholm, Sweden
[12] Astrophysics Research Institute, Liverpool John Moores University, Liverpool Science Park, 146 Brownlow Hill, Liverpool L3 5RF, UK
[13] Department of Astronomy, Kyoto University, Kitashirakawa-Oiwake-cho, Sakyo-ku, Kyoto 606-8502, Japan
[14] McWilliams Center for Cosmology, Department of Physics, Carnegie Mellon University, Pittsburgh, PA 15213, USA
[15] Tuorla Observatory, Department of Physics and Astronomy, FI-20014 University of Turku, Finland
[16] Finnish Centre for Astronomy with ESO (FINCA), FI-20014 University of Turku, Finland
[17] Division of Physics, Mathematics and Astronomy, California Institute of Technology, Pasadena, CA 91125, USA
[18] Department of Physics and Astronomy, Purdue University, 525 Northwestern Ave., West Lafayette, IN 47907, USA
[19] Department of Physics and Astronomy, University of North Carolina at Chapel Hill, Chapel Hill, NC 27599-3255, USA
[20] The Oskar Klein Centre, Department of Astronomy, Stockholm University, AlbaNova, SE-10691 Stockholm, Sweden
[21] Department of Particle Physics and Astrophysics, Weizmann Institute of Science, 76100 Rehovot, Israel
[22] Centre for Astrophysics and Supercomputing, Swinburne University of Technology, John St., Hawthorn, VIC 3122, Australia
[23] ARC Centre of Excellence for Gravitational Wave Discovery (OzGrav), John St., Hawthorn, VIC 3122, Australia
[24] Department of Astrophysical Sciences, 4 Ivy Lane, Princeton University, Princeton, NJ 08540, USA
[25] Department of Physics, Drexel University, Philadelphia, PA 19104, USA
[26] School of Physics and Astronomy, University of Minnesota, Minneapolis, MN 55455, USA

Abstract

We present optical, radio, and X-ray observations of EP250108a/SN 2025kg, a broad-line Type Ic supernova (SN Ic-BL) accompanying an Einstein Probe (EP) fast X-ray transient at $z = 0.176$. EP250108a/SN 2025kg possesses a double-peaked optical light curve, and its spectrum transitions from a blue underlying continuum to a typical SN Ic-BL spectrum over time. We fit a radioactive decay model to the second peak of the optical light curve and find SN parameters that are consistent with the SN Ic-BL population, while its X-ray and radio properties are consistent with those of low-luminosity GRB (LLGRB) 060218/SN 2006aj. We explore three scenarios to understand the system's multiwavelength emission: (a) SN ejecta interacting with an extended circumstellar medium (CSM), (b) the shocked cocoon of a collapsar-driven jet choked in its stellar envelope, and (c) the shocked cocoon of a collapsar-driven jet choked in an extended CSM. Models (b) and (c) can explain the optical light curve and are also consistent with the radio and X-ray observations. We favor model (c) because it can self-consistently explain both the X-ray prompt emission and first optical peak, but we do not rule out model (b). From the properties of the first peak in model (c), we find evidence that EP250108a/SN 2025kg interacts with an extended CSM and infer an envelope mass $M_e \sim 0.1\ M_\odot$ and radius $R_e \sim 4 \times 10^{13}$ cm. EP250108a/SN 2025kg's multiwavelength properties make it a close analog to LLGRB 060218/SN 2006aj and highlight the power of early follow-up observations in mapping the environments of massive stars prior to core collapse.

Unified Astronomy Thesaurus concepts: Type Ic supernovae (1730); Gamma-ray bursts (629); Circumstellar matter (241)

1. Introduction

γ-ray missions have discovered thousands of γ-ray bursts (GRBs), whose populations are relatively well characterized (T. Piran 2004). However, satellites sensitive to soft X-rays (HETE-2's Wide-field X-ray Monitor, Beppo-Sax, ∼2–25 keV; MAXI, ∼0.5–30 keV) have found a much smaller number of

bursts (J. Heise et al. 2001; T. Sakamoto et al. 2005; H. Negoro et al. 2016) with peak energies below those of classical GRBs (hundreds of keV). The origins of these fast extragalactic X-ray transients (FXTs) and X-ray flashes (XRFs)[27] are an open question. Some possibilities include high-z (J. Heise et al. 2001) or off-axis (J. E. Rhoads 1997; P. Mészáros et al. 1998) GRBs; "dirty fireballs," or baryon-loaded GRBs with low Lorentz factors (C. D. Dermer et al. 1999); supernova (SN) shock breakout (SBO) or cooling (S. A. Colgate 1974; S. Balberg & A. Loeb 2011); tidal disruption events (TDEs; J. Quirola-Vásquez et al. 2022); off-axis GRBs (N. Sarin et al. 2021); magnetars after binary neutron star mergers (D. Lin et al. 2022; J. Quirola-Vásquez et al. 2024); or new, exotic classes of transient phenomena. The archival nature of most FXTs' discoveries and lack of real-time follow-up (J. Quirola-Vásquez et al. 2022) made their characterizations historically difficult.

The Tianguan Telescope, or Einstein Probe (EP; W. Yuan et al. 2015, 2018, 2022, 2025), is changing the landscape of X-ray time domain science with its wide-field, soft X-ray capabilities. EP possesses an all-sky monitor (ASM) Wide-field X-ray Telescope (WXT) that has an instantaneous field of view of 3600 deg^2, operating from 0.4 to 5 keV. It has over 100 times the field of view of MAXI (M. Matsuoka et al. 2009), the only other currently operational X-ray ASM. In addition to WXT, EP also possesses two conventional X-ray focusing telescopes operating from 0.3 to 10 keV that can provide arcsecond localizations.

In its first year of operations, EP has already found a multitude of extragalactic FXTs, many of which have possible relations to GRBs and XRFs. EP 240219a was interpreted as an X-ray-rich (stronger X-ray than γ-ray emission) GRB (Y.-H. I. Yin et al. 2024). EP 240315a had an optical and radio counterpart and likely originated from an long GRB (LGRB; Y. Liu et al. 2025; R. Ricci et al. 2025) or a relativistic TDE (J. H. Gillanders et al. 2024). EP 240408A had no accompanying γ-ray emission, and its X-ray properties are inconsistent with most known transient classes (W. Zhang et al. 2025). Possible origins include a white dwarf disrupted by an intermediate-mass black hole or an exotic GRB (B. O'Connor et al. 2025). EP 240801a was a confirmed XRF and was interpreted as either an off-axis or intrinsically weak jet (S.-Q. Jiang et al. 2025). EP 241021a had no accompanying γ-ray emission and also had a very luminous optical and radio counterpart (M. Busmann et al. 2025; G. Gianfagna et al. 2025; G.-L. Wu et al. 2025; S. Xinwen et al. 2025; M. Yadav et al. 2025). Its interpretation is also not clear, though refreshed GRB shocks accompanying a low-luminosity GRB (LLGRB) have been proposed as one scenario (M. Busmann et al. 2025), as well as a compact star merger producing a compact object or binary compact object system (G.-L. Wu et al. 2025), intermediate mass black hole tidal disruption event (S. Xinwen et al. 2025), off-axis jet (G. Gianfagna et al. 2025; S. Xinwen et al. 2025), and more.

In addition, EP has discovered a few events that show clear SN associations, with a range of interpretations in the literature. EP 240414a (H. Sun et al. 2025; H. Hamidani et al. 2025b; S. Srivastav et al. 2025; J. N. D. van Dalen et al. 2025; J.-H. Zheng et al. 2025) is one such event. It had no accompanying γ-ray emission, and its peak energy was determined to be <1.3 keV, making it an XRF. Its optical counterpart was a broad-lined Type Ic SN (SN Ic-BL), the type of SN found observationally associated with long GRBs (see, e.g., T. J. Galama et al. 1998; J. Hjorth et al. 2003; Z. Cano et al. 2017). It also possessed a mysterious red peak prior to the SN, which was described as the interaction of a GRB jet with a dense circumstellar medium (CSM; J. N. D. van Dalen et al. 2025), shock cooling emission (SCE) following interaction with a dense CSM (H. Sun et al. 2025), afterglow from a mildly relativistic cocoon (H. Hamidani et al. 2025b) or off-axis jet (J.-H. Zheng et al. 2025), or refreshed shocks from a GRB (S. Srivastav et al. 2025). There have also been suggested resemblances (J. N. D. van Dalen et al. 2025) to luminous fast blue optical transients (LFBOTs; M. R. Drout et al. 2014; S. J. Prentice et al. 2018; M. Pursiainen et al. 2018; R. Margutti et al. 2019; D. A. Perley et al. 2019; A. Y. Q. Ho et al. 2023) due to its rise time, though its red colors indicate otherwise. Recently, EP 250304a showed spectroscopic evidence that its optical counterpart was also an SN Ic-BL (L. Izzo et al. 2025) while possessing no associated γ-ray emission (M. E. Ravasio et al. 2025a).

Multiwavelength studies of EP events with associated SNe Ic-BL are integral to understanding the link between FXTs, XRFs, GRBs, SNe, and other classes of high-energy phenomena. In this Letter, we present EP250108a/SN 2025kg (R. Eyles-Ferris 2025a), an EP transient without associated γ-ray emission and an SN Ic-BL optical counterpart, displaying a double-peaked light curve (LC). At the time of writing this Letter, two papers on this source have been published on arXiv, R. A. J. Eyles-Ferris et al. (2025) and J. C. Rastinejad et al. (2025). R. A. J. Eyles-Ferris et al. (2025) study the initial optical peak up to 6 days after the X-ray burst in addition to the X-ray and radio data, while J. C. Rastinejad et al. (2025) study the accompanying SN Ic-BL from 6 days to 66.5 days after the X-ray burst. We provide comparisons of our analysis to each of these two works throughout the Letter. Furthermore, we note that during the referee process, W. X. Li et al. (2025c) also published their paper on arXiv. W. X. Li et al. (2025c) is from the EP science team and presents the full prompt emission analysis (which was not available publicly at the time we submitted this work), in addition to characterizing the optical counterpart. Because this work was published during the referee process, we do not provide as detailed comparisons to their work as we do to R. A. J. Eyles-Ferris et al. (2025) and J. C. Rastinejad et al. (2025), but we still do compare important results when relevant.

The Letter is structured as follows. In Section 2, we present the optical photometry and spectroscopy, as well as radio and X-ray observations of EP250108a/SN 2025kg; in Section 3, we present the analysis of these observations; in Section 4, we model the optical light curve; in Section 5, we estimate the prompt X-ray signal from the different models we tested; in Section 6, we discuss the implications of our results; and in Section 7, we provide a summary. We note that throughout this Letter, we utilize a flat ΛCDM cosmology with $\Omega_m = 0.315$ and $H_0 = 67.4\,\mathrm{km\,s^{-1}\,Mpc^{-1}}$ (Planck Collaboration et al. 2020) to

---

[27] In the literature, there are often contradictions between how FXTs and XRFs are defined. We define FXTs as short flashes of X-ray emission that last a few minutes to a couple of hours that are discovered in the soft X-rays (0.3–10 keV). We define XRFs as bursts of X-rays with true peak energies $E_p \lesssim 25$ keV. Therefore, an FXT need not be an XRF, as they are defined by their discovered energy range, not their true peak energy. On the other hand, many XRFs are part of the FXT population, as long as their peak energy is between 0.3 and 10 keV.

convert the redshift to a luminosity distance and correct for the Milky Way extinction of $E(B - V)_{MW} = 0.02$ mag (E. F. Schlafly & D. P. Finkbeiner 2011) using the J. A. Cardelli et al. (1989) extinction law with $R_v = 3.1$.

2. Observations

In this section, we present the observations used in our analysis of EP250108a/SN 2025kg. Hereafter, we refer to T_0 as the beginning time of the X-ray prompt detection, or UT 2025 January 8 12:30:28.34. The X-ray and γ-ray observations presented in Section 2.1 are taken from General Coordinate Networks (GCNs),[28] and we also supplement our optical photometry with observations from GCNs at early times (R. Eyles-Ferris 2025b; L. Izzo 2025; A. Kumar et al. 2025; A. S. Moskvitin et al. 2025; Z. P. Zhu et al. 2025; X. Zou et al. 2025), as our photometry only begins at $T_0 + 3.3$ days. We will make all of our observations publicly available on WISeREP upon publication (O. Yaron & A. Gal-Yam 2012). We provide a log of the spectroscopic observations and the photometric observations in the Appendix.

2.1. X-Ray and γ-Ray Observations

The WXT on EP triggered on EP250108a on UT 2025 January 8 12:30:28.34 at a location α (J2000) = 55°.623 and δ (J2000) = −22°.509 with an uncertainty radius of 2′.2 (R. Z. Li et al. 2025a). According to R. Z. Li et al. (2025a), the event lasted more than 2500 s, possessing a peak flux in the 0.5–4 keV band of 1.4×10^{-10} erg cm^{-2} s^{-1} and a time-averaged flux of $6.38^{+22.52}_{-3.00} \times 10^{-11}$ erg s^{-1} cm^{-2}. However, the prompt emission analysis from the EP science team presented in W. X. Li et al. (2025c) reports that the event lasted 960^{+3092}_{-208} s, with the large error bars due to an interruption in later observations due to the Earth's occultation.

Given the redshift $z = 0.176$ determined through optical spectroscopy (Z. P. Zhu et al. 2025b; corresponding to a distance of 881 Mpc), the peak flux corresponds to a peak X-ray isotropic-equivalent luminosity of $\sim 1.3 \times 10^{46}$ erg s^{-1} and an average isotropic-equivalent luminosity of $5.92^{+20.88}_{-2.77} \times 10^{45}$ erg s^{-1}. The source was followed up by EP's onboard follow-up X-ray telescope at UT 2025 January 9 10:42:46, 22.1 hr after the WXT trigger. No source was detected in 0.5–10 keV to an upper limit of 3×10^{-14} erg cm^{-2} s^{-1} (R. Z. Li et al. 2025b). The source was also followed up with the Neil Gehrels Swift Observatory's X-ray Telescope (N. Gehrels et al. 2004; D. N. Burrows et al. 2005) on UT 2025 January 10 15:17:00, 2.12 days after the WXT trigger. A source was not detected in 0.3–10 keV to an upper limit of 3.8×10^{-3} counts s^{-1} (A. J. Levan et al. 2025a). For a canonical counts-to-flux conversion of 4×10^{-11} given the lack of an X-ray spectrum at this time, this count rate upper limit corresponds to a flux upper limit of 1.5×10^{-13} erg cm^{-2} s^{-1}.

At the time of the burst, the burst's location was occulted by the Earth (M. E. Ravasio et al. 2025b) to Fermi's Gamma-Ray Burst Monitor (C. Meegan et al. 2009). The location was visible 415 s after the burst, and assuming a Band function spectrum with $E_{peak} = 70$ keV, $\alpha = -1.9$, $\beta = -3.7$, and a duration of 8.192 s, the most conservative sky-averaged upper limit is a flux of 2.6×10^{-8} erg cm^{-2} s^{-1} from 10 to 1000 keV (M. E. Ravasio et al. 2025b). At a redshift $z = 0.176$, this

corresponds to an isotropic luminosity upper limit of 2.4×10^{48} erg s^{-1}, or an isotropic energy upper limit of 2.0×10^{49} erg. Because the field was only visible shortly after the burst, these values cannot be taken as a strict upper limits for the prompt emission. However, these values are very low in comparison to those derived for classical GRBs and are similar to LLGRBs ($L_{iso} < 10^{49}$ erg s^{-1}; E. Liang et al. 2007; F. J. Virgili et al. 2009).

2.2. Liverpool Telescope

We obtained Liverpool Telescope (LT; I. A. Steele et al. 2004) observations with the IO:O camera in the Sloan Digital Sky Survey g, r, and i filters at multiple epochs, starting at 3 days post EP trigger. Basic reductions (bias subtraction, flat-fielding, and astronomy) were provided by the automatic IO:O pipeline, and these reduced images were downloaded from the LT archive. The signal-to-noise of the first three epochs is low due to poor observing conditions, and a small number of frames affected by tracking errors or with very poor seeing were discarded. The remaining frames were stacked using the SWarp software (E. Bertin 2010). Point-spread function (PSF) photometry on obtained stacks was performed with the use of SExtractor (E. Bertin & S. Arnouts 1996) and PSFex (E. Bertin 2013) relative to the Panoramic Survey Telescope and Rapid Response System 1 (Pan-STARRS1) catalog (K. C. Chambers et al. 2016). In Figure 1, we show the LT images taken 9.3 days after the explosion, along with the Pan-STARRS1 reference images.

2.3. NOT

The AUTOPHOT (S. J. Brennan & M. Fraser 2022) pipeline was employed to perform photometric measurements on Nordic Optical Telescope (NOT)/ALFOSC images. For each image, the World Coordinate System values were verified using ASTROMETRY.NET (D. Lang et al. 2010). An effective PSF model was constructed using bright, isolated sources in the image with the Photutils package (L. Bradley et al. 2024). Zero-points were calibrated against sequence sources in the ATLAS All-Sky Stellar Reference Catalog (J. L. Tonry et al. 2018) for Sloan $griz$ images.

Science and reference images from Pan-STARRS1 were aligned using SWarp, and reference image subtraction was performed utilizing the saccadic fast Fourier transform (SFFT) algorithm (L. Hu et al. 2022) to isolate transient flux.

2.4. IMACS

We observed one epoch of Sloan g-, r-, and i-band images of SN 2025kg with the Inamori–Magellan Areal Camera and Spectrograph (IMACS; A. Dressler et al. 2011) on 2025 February 5. The images were reduced using standard procedures, including bias subtraction and flat-fielding. We performed PSF photometry on the reduced images and calibrated the photometry relative to the Pan-STARRS1 catalog (K. C. Chambers et al. 2016).

2.5. GHTS

We obtained two epochs of long-slit spectroscopy of SN 2025kg with the Goodman High Throughput Spectrograph (GHTS; J. C. Clemens et al. 2004) mounted on the Southern Astrophysical Research (SOAR) telescope on 2025 January 18 and 2025 January 23. The observations consisted of 6×600 s

---
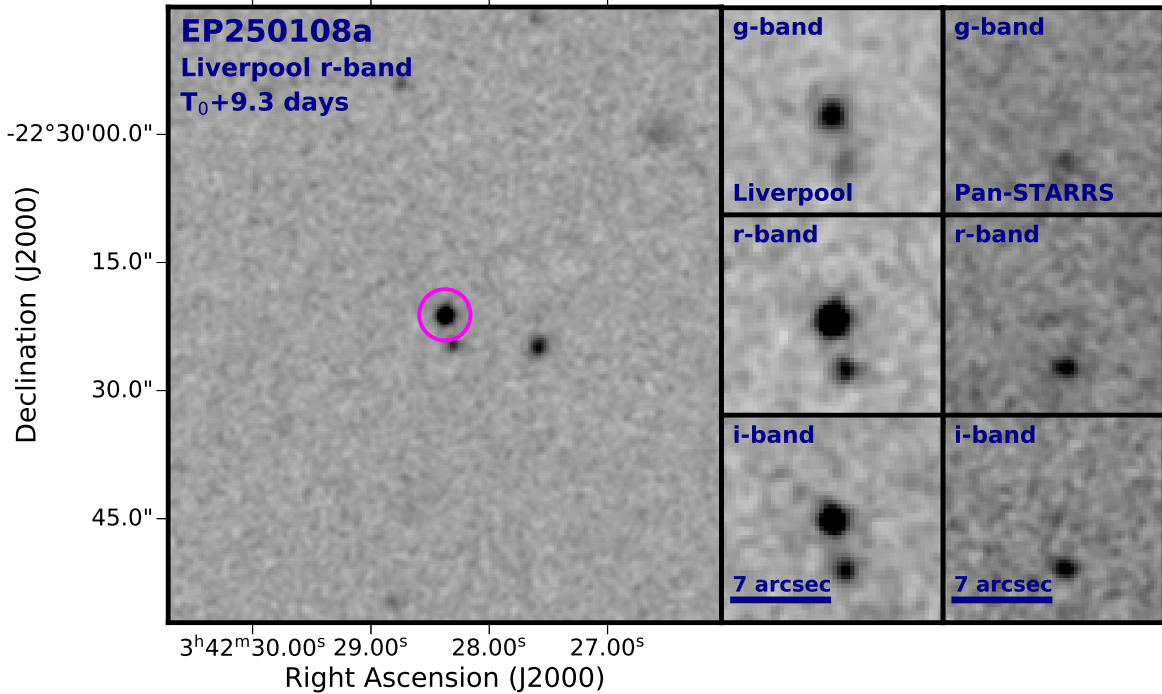
Figure 1. LT images of EP250108a/SN 2025kg. The large left panel shows the wider field of view of EP250108a in the r band 9.3 days after T_0. The right panels show the observations taken in the g, r, and i bands, as well as the Pan-STARRS1 templates used for photometry. The host galaxy is faint ($r \sim 23.2$; A. Dey et al. 2019), so image subtraction is not necessary until the final epoch. Images have been smoothed for display purposes.

of exposures. Both observations were taken with a grating of 400 lines mm^{-1} and a $1''.0$ wide slit mask in the M1 spectroscopic setup (hereafter 400M1) with 2×2 binning using the GHTS red camera. The 400M1 spectra cover a wavelength range of 3800–7040 Å.

The spectra were reduced using `pypeit` (J. X. Prochaska et al. 2020b, 2020a), using arcs taken immediately before and/or after target observation and calibration images from the same night. Flux calibration was performed using standard stars observed on the night of the observations with an identical 400M1 setup and 2×2 binning.

We also imaged the location of SN 2025kg on 2025 January 23 and 31 with SOAR/GHTS in imaging mode. We took three 60 s exposures each in the g and r bands on the first epoch and six 90 s exposures each in the g and r bands on the second epoch. After bias correction, flat-fielding, background subtraction, and astrometric correction using ASTROMETRY.NET (D. Lang et al. 2010), the images were stacked with SWARP (E. Bertin 2010). We performed image subtraction on the stacked images using SFFT with an archival template from the DECam Legacy Survey (A. Dey et al. 2019). Aperture photometry was conducted with SEXTRACTOR (E. Bertin & S. Arnouts 1996), and zero-points were measured from the Pan-STARRS1 catalog (K. C. Chambers et al. 2016).

2.6. LRIS

We obtained one epoch of long-slit spectroscopy of SN 2025kg on 2025 January 25 with the Keck Observatory Low Resolution Imaging Spectrometer (LRIS; J. B. Oke et al. 1995). This observation consisted of 3×900 s exposures on both the blue and red sides using a $1''.0$ slit mask. We used the 400/3400 grating for the blue exposures and the 400/8500 grating for the red exposures, and the spectrum had

wavelength coverage of 3000–9300 Å. These observations were reduced using LPipe (D. A. Perley 2019).

2.7. Binospec

We obtained one epoch of long-slit spectroscopy of SN 2025kg with Binospec (D. Fabricant et al. 2019) on the MMT Observatory 6.5 m telescope on 2025 February 3. The observation consisted of 3×900 s exposures. The data were acquired with a grating of 270 lines mm^{-1} and a $1''.0$ slit mask. The basic data processing (bias subtraction, flat-fielding) is done using the Binospec pipeline (J. Kansky et al. 2019). The processed images are downloaded from the MMTO queue observation data archive. The spectra are reduced with IRAF, including cosmic-ray removal, wavelength calibration (using arc lamp frames taken immediately after the target observation), and relative flux calibration with archived spectroscopic standard observation. The Binospec spectrum has a wavelength coverage of 3900–9240 Å.

2.8. GMOS

SN 2025kg was observed using the GMOS (I. M. Hook et al. 2004; G. Gimeno et al. 2016) long slit at the Gemini South telescope in Cerro Pachon, Chile, on the nights of 2025 January 13, 23, and 29. The grating B480 was used at a central wavelength of 5400/5450 Å with 2×2 binning, giving wavelength coverage of around 3800–7500 Å at $R \sim 1400$. The observations consisted of 4×600 s exposures, except for January 29 (4×420 s). A standard data reduction process was performed using the Gemini DRAGONS package (K. Labrie et al. 2023), resulting in wavelength- and flux-calibrated spectra.
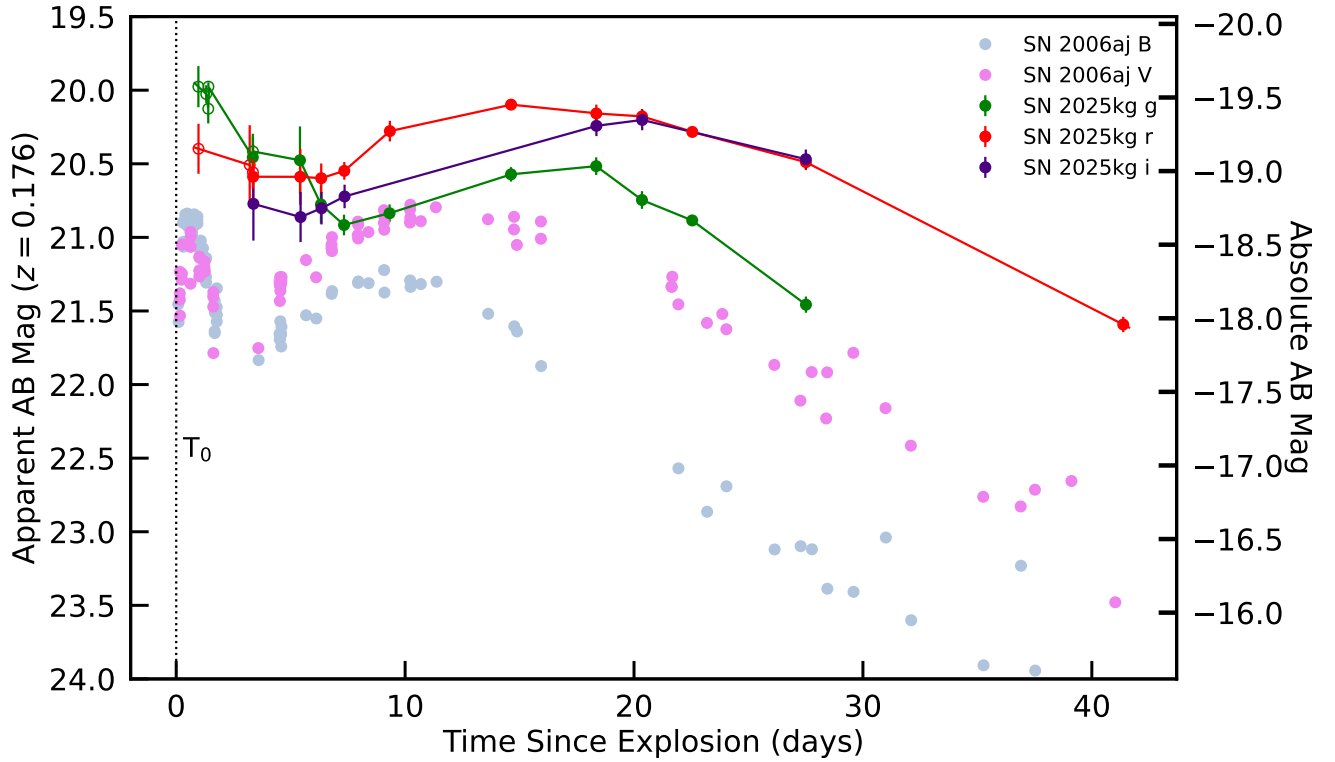
Figure 2. Light curve of SN 2025kg in the *g*, *r*, and *i* bands connected with a curve, where all measurements have been corrected for Milky Way extinction and times are in the observer frame. Open circles are photometry points taken from GCNs, while filled circles are photometry taken from our observations. For comparison, we show the *B*- and *V*-band light curves of SN 2006aj (M. Modjaz et al. 2006; F. B. Bianco et al. 2014; P. J. Brown et al. 2014), also corrected for Milky Way extinction, transformed to the redshift of SN 2025kg ($z = 0.176$). We also show the absolute magnitudes on the right axes. SN 2025kg's light curve displays very similar features to SN 2006aj, though it is more luminous and evolves more slowly.

Table 1
VLA Observations of EP 250108A

δt_{obs} (days)	ν_{obs} (GHz)	Beam Size (arcsec)	Beam Angle (deg)	VLA Configuration	F_ν[a] (μJy)	Image rms (μJy)
6.5	10.0	0.41×0.17	-30.0	A	$\leqslant 13.5$	4.5
25.56	10.0	0.34×0.17	0.7	A	$\leqslant 13.5$	4.5
47.53	10.0	15.03×5.65	3.5	A→D	$\leqslant 19.8$	6.6
52.51	10.0	10.75×5.41	8.7	D	$\leqslant 16.5$	5.5

Note.
[a] Upper limits correspond to 3σ.

2.9. Very Large Array

We observed the location of EP250108a with NSF's Karl G. Jansky Very Large Array (VLA) on 2025 January 15 at a midtime of 00:53 UT ($\delta t = 6.5$ days postdiscovery) at a midfrequency of 10 GHz (4 GHz bandwidth) for a total of 0.6 hr on source (program 25A-374; PI: Perley). We used J0329–2357 for phase and gain calibration and 3C 147 for flux and bandpass calibration. Data reduction and imaging was performed using the Common Astronomy Software Applications (J. P. McMullin et al. 2007) VLA Calibration Pipeline[29] and the VLA Imaging Pipeline.[30] No source was detected at or near the position of EP250108a/SN 2025kg in this observation. We used the program pwkit/imtool (P. K. G. Williams et al. 2017) to measure the rms of the image and determine

a 3σ upper limit on a radio counterpart of $F_\nu \lesssim 13.5\,\mu$Jy (G. Schroeder et al. 2025). We initiated three additional VLA epochs at 25.6, 47.5, and 52.5 days and did not detect any sources at the position of EP250108a/SN 2025kg. A summary of these observations is presented in Table 1.

3. Analysis

3.1. Light-curve Analysis

We show the *gri* light curve of EP250108A/SN 2025kg in Figure 2. The light curve clearly has two peaks. The first peak rises on a timescale of less than 1 day after T_0 and displays blue colors ($g - r = -0.4$ mag) and then declines until 5 days after T_0 (though this decline extends until day 8 in the *g* band). Initially, the rapid rise, blue colors, and luminous ($M_g \sim -19.5$ mag) emission led some authors to draw a connection with LFBOTs (Z. P. Zhu et al. 2025a). However, there was a

---

transition to red colors along with a slower rise after the initial decline, behavior that has never been seen in an LFBOT but has been seen in certain SNe with early shock-powered peaks.

We spectroscopically confirm an SN Ic-BL classification during the later phase of the optical light curve in Section 3.3. The SN Ic-BL, SN 2025kg (A. J. Levan et al. 2025b), rises to maximum light during its second peak on a timescale of ∼15 days in the r band and 18 days in the g band. The peak absolute magnitudes ($M_r = -19.39 \pm 0.02$, $M_g = -18.95 \pm 0.06$) are brighter than the average SN Ic-BL population ($M_r = -18.5 \pm 0.9$ mag; F. Taddia et al. 2019; G. P. Srinivasaragavan et al. 2024a) but are still within the overall range seen for SNe Ic-BL in the literature (−16.86 to −20.9 mag; F. Taddia et al. 2019; G. P. Srinivasaragavan et al. 2024a) and consistent with GRB SNe (e.g., GRB 980425/SN 1998bw, $M_R = -19.36 \pm 0.05$, T. J. Galama et al. 1998; GRB 230812B/SN 2023pel, $M_r = -19.46 \pm 0.18$ mag, G. P. Srinivasaragavan et al. 2024b).

K. K. Das et al. (2024) found an empirical correlation between the first peak and second peak in a sample of stripped-envelope SNe (which included two SNe Ic-BL) where the mechanism used to describe the first peak was SCE from SN ejecta interacting with an extended CSM (A. L. Piro et al. 2021). This correlation is $M_2 = 0.8 \times M_1 - 4.7$, where M_1 and M_2 are the absolute magnitudes of the first and second peak, respectively, in the r band. Utilizing this expression, given the brightness of the second peak, we expect the first peak to have a brightness of $M_r \sim -18.4$ mag. The first peak is brighter than expected from the correlation, with $M_r \sim -19.1$ mag. This is not surprising, as only two SNe Ic-BL were in the sample that K. K. Das et al. (2024) used to create this correlation. However, it is notable that the overall trend is still followed, where the first peak is more luminous than the second peak.

In Figure 2, we also show the light curve of SN 2006aj (M. Modjaz et al. 2006; F. B. Bianco et al. 2014; P. J. Brown et al. 2014), shifted to the redshift of SN 2025kg, with the cosmological correction for redshift implemented on the magnitudes. SN 2006aj is an SN Ic-BL linked to the LLGRB 060218 that shows a similar double-peaked optical light curve and soft X-ray prompt emission (S. Campana et al. 2006; P. Ferrero et al. 2006; N. Mirabal et al. 2006; E. Pian et al. 2006; A. M. Soderberg et al. 2006; J. Sollerman et al. 2006) as EP250108a/SN 2025kg. Though we do not show the light curve in the figure for visual purposes, we also compare the light curve to that of SN 2020bvc (A. Y. Q. Ho et al. 2020). SN 2020bvc is an SN Ic-BL found independently of a high-energy trigger (A. Y. Q. Ho et al. 2020; L. Izzo et al. 2020; J. Rho et al. 2021) that also displays a similar double-peaked light curve and possesses X-ray and radio emission similar to other LLGRBs.

SN 2006aj's and SN 2020bvc's first peak fades on a timescale of around 1 day, which is significantly faster than the fading timescale for SN 2025kg. Furthermore, the peak absolute magnitudes of this first peak are significantly fainter for SN 2006aj ($M_B \sim -18.5$ mag) and SN 2020bvc ($M_g \sim -18.1$ mag). We note here that the first peaks derived for both SN 2025kg and SN 2020bvc may not be the true "peak," as both events are fading after their first detection. Therefore, the true peak might be more luminous and earlier than the first detection. The second peaks are also fainter, as SN 2006aj possesses a peak $M_V \sim -18.8$ mag (P. Ferrero et al. 2006), and SN 2020bvc possesses a peak $M_r \sim -18.7$ mag.

Later on the text, we also compare SN 2025kg's properties to those of iPTF 16asu (L. Whitesides et al. 2017) and SN 2018gep (A. Y. Q. Ho et al. 2019; S.-C. Leung et al. 2021; T. A. Pritchard et al. 2021). These SNe were SNe Ic-BL found independent of high-energy triggers and did not display a clear double peak in their light curves. However, their quick rise times, luminous peaks, and blue colors at peak indicate a likely additional powering mechanism making contributions to the early-time light curve (more in Section 4), justifying the comparison with SN 2025kg.

3.2. Bolometric Luminosity Light Curve

We create SN 2025kg's bolometric luminosity light curve through utilizing bolometric correction (BC) coefficients (J. D. Lyman et al. 2014, 2016). We have sparse i-band photometric coverage of SN 2025kg (see Figure 2) but sufficient coverage in the g and r bands over numerous epochs. Therefore, we can utilize the BC coefficients, which depend on $g - r$ colors, to compute a bolometric luminosity light curve. These coefficients were measured by fitting the spectral energy distributions of a large sample of stripped-envelope SNe with broadband coverage across the ultraviolet, optical, and infrared wavelengths and can be utilized to convert between $g - r$ colors and an absolute bolometric magnitude. We note that SNe Ic-BL may have slightly different color evolution than that of other stripped-envelope SNe; however, the BC coefficients were calculated with a few SNe Ic-BL in the overall data set (J. D. Lyman et al. 2014), and most sample papers of SNe Ic-BL (F. Taddia et al. 2019; A. Corsi et al. 2023; S. Anand et al. 2024; G. P. Srinivasaragavan et al. 2024a) use this method to calculate bolometric luminosity LCs. We use two different BC coefficients in our analysis—one for the shock cooling phase and one for the radioactive decay phase, both from J. D. Lyman et al. (2014). The BC coefficient for the shock cooling phase is described as

$$\text{BC}_g = -0.146 + 0.479 \times (g - r) - 2.257 \times (g - r)^2. \tag{1}$$

We note that this coefficient was not calculated specifically for stripped-envelope SNe, as there was a lack of sufficient events to do so. The BC coefficient for stripped-envelope SNe in the radioactive decay phase is

$$\text{BC}_g = 0.054 - 0.195 \times (g - r) - 0.719 \times (g - r)^2, \tag{2}$$

with $-0.3 \text{ mag} < g - r < 1.0 \text{ mag}$. We note that we have one r-band point at $T_0 + 41$ days that does not have an accompanying g-band point. We extrapolate the g-band light curve using the scipy.interp1d package to obtain a g-band photometric point to use for the creation of a bolometric luminosity at late times. We then calculate the BC_g coefficient for every epoch in our sample where we have simultaneous r- and g-band observations. Finally, using the definition of BC coefficients,

$$\text{BC}_x = M_{\text{bol}} - M_x, \tag{3}$$

we calculate the absolute bolometric magnitude light curve and convert to a bolometric luminosity light curve given the distance luminosity at $z = 0.176$. We present the bolometric luminosity light curve in Figure 3 and compare it to SN 2006aj, SN 2020bvc, and SN 2018gep. Similar to the
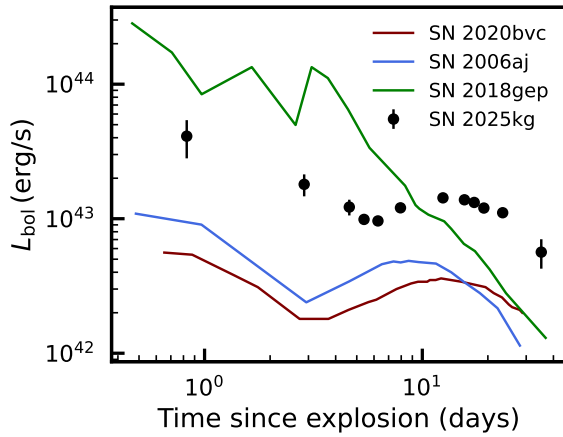
Figure 3. Bolometric luminosity LC of SN 2025kg, compared to SN 2006aj (M. Modjaz et al. 2006; F. B. Bianco et al. 2014; P. J. Brown et al. 2014), SN 2020bvc (A. Y. Q. Ho et al. 2020), and SN 2018gep (A. Y. Q. Ho et al. 2019; S.-C. Leung et al. 2021; T. A. Pritchard et al. 2021), with times in the rest frame. SN 2025kg's bolometric luminosity LC has a very similar shape to that of SN 2006aj and SN 2020bvc while being more luminous and evolving on a slightly slower timescale. SN 2018gep does not have a double peak and has a higher initial luminosity, but it has a more rapid decline in luminosity over time.

photometry in Figure 2, the peak bolometric luminosity of the first peak and second peak are significantly larger than those of the other two compared events, while evolving on slower timescales. SN 2018gep does not display a double-peaked LC and has a more luminous peak, though its luminosity declines much more rapidly than the other three events.

3.3. Spectral Analysis

We obtained seven spectra of SN 2025kg up to 26 days after T_0 and present them in Figure 4. Here we discuss the spectroscopic evolution, along with comparisons to other similar events.

A close-up of the first spectrum is shown in Figure 5, along with spectra of SN 2006aj (M. Modjaz et al. 2006) and SN 2020bvc (A. Y. Q. Ho et al. 2020) at similar epochs. The spectrum displays an underlying blue continuum and is best fit with a blackbody with $L_{bol} = (1.60 \pm 0.31) \times 10^{43}$ erg s^{-1}, $T_{BB} = (13.69 \pm 3.64) \times 10^3$ K, and $R_{BB} = (1.11 \pm 0.10) \times 10^{15}$ cm. SN 2025kg is significantly hotter than SN 2006aj and SN 2020bvc at similar phases. Since the initial radius of the progenitor is $\ll R_{BB}$, the mean velocity over the first 3.9 (rest-frame) days is therefore 1.1×10^{15} cm/3.9 $\sim 0.1c$. This is the same mean velocity that was derived for SN 2020bvc during the first 1.8 days (A. Y. Q. Ho et al. 2020). Therefore, since the photospheric velocity slows with time, this means that SN 2025kg has relatively faster moving ejecta than SN 2020bvc at earlier times (which we also later confirm with explicit velocity measurements).

Furthermore, we also identify a possible broad absorption feature in SN 2025kg's first spectrum centered around 4100 Å that peaks at 4500 Å, which could be due to a blueshifted Fe II absorption feature (rest-frame 5169 Å), commonly seen in SNe Ic-BL. The photospheric velocity inferred from this feature is $\sim 0.1c$ (see Table 2), which is consistent with the speed derived from the blackbody fitting. This feature is also present in SN 2006aj's and SN 2020bvc's spectra.

However, this line identification is not robust, for multiple reasons. First, there is an emission feature around 4100 Å that

we determine is not a real feature, as it is due to noisy spikes in the spectra. Therefore, the slight undulation between 3800 and 4800 Å must be interpreted with caution. Furthermore, at the blackbody temperature that we derive ($>13,000$ K), Fe has mostly transitioned from Fe II to Fe III (P. Nugent et al. 1995). In addition, at the high velocities that we derive for the Fe II feature later in this section, the Fe II 5169 Å feature may be blended with the Fe II features at 5018 and 4924 Å. Finally, in Section 4, we show that the optical flux during the time of the first spectral epoch (4.6 days) has contributions from an additional component (CSM interaction or a shocked cocoon) than just the radioactive decay of nickel. If the flux is dominated by this additional component, it is surprising that a photospheric Fe line would be a dominant feature in the spectra; however, there are still strong contributions from the radioactive decay of nickel during this epoch, so the possibility that a photospheric Fe line exists is still relevant. There is also a possible emission feature at around 4500 Å, which may be due to [Mg I] at 4571 Å, though this feature is usually strong at later phases. However, due to the noise in the spectra, this interpretation must also be taken with caution.

K. Maeda et al. (2023) compute synthetic spectra of engine-driven explosions with brief energy injection from the central engine and find in their models that a peak in the early-time (<7 days after explosion) spectrum at 4500 Å and the lack of a peak between 5500 and 6000 Å are indicative of a higher-velocity component in the ejecta ($>60,000$ km s^{-1}) that is greater than the normal photospheric velocity at the time. We see this same behavior in SN 2025kg, which points toward a higher-velocity component at early times, giving evidence that a collapsar jet-driven system may be necessary to explain SN 2025kg's properties (more in Section 6).

SN 2025kg's spectra turn redder with time, and further broad absorption features develop like Si II (rest-frame 6347 Å), along with the continued lack of H and He features. We run the GHTS spectrum 9.6 days after T_0 in the Supernova Identification Code (S. Blondin & J. L. Tonry 2007) and find that the best-fit spectrum is SN Ic-BL 2002ap (P. A. Mazzali et al. 2002), and the spectra at later phases continue to show SN Ic-BL matches, allowing for a classification. We also show a spectrum 15 days after T_0, during the SN's peak light in the r band in Figure 5, along with SN 2006aj's and SN 2020bvc's spectra at similar phases. We see clear broad absorption features in the spectrum blueshifted with characteristic velocities. We label the Fe II and Si II features, which are good indicators of the photospheric velocity (M. Modjaz et al. 2016). By eye, we see that the absorption troughs for the Fe II feature in both SN 2025kg and SN 2006aj are centered around 5000 Å, and they are around 4800 Å for SN 2020bvc. This indicates that SN 2020bvc has a higher photospheric velocity near peak, even though it had a slower velocity at earlier times.

We then measure the equivalent width (EW) of the Na I absorption doublet (5890, 5896 Å) using the LRIS spectrum at 17.7 days after T_0. This feature is known to be a proxy for the amount of host-galaxy extinction present in systems (M. D. Stritzinger et al. 2018). We can convert the EW to a host-galaxy extinction value through the relation from M. D. Stritzinger et al. (2018): A_V^{host} [mag] $= 0.78(\pm 0.15) \times EW_{Na I}$. But D. Poznanski et al. (2011) showed that when using low-resolution spectra, a large scatter exists in the correlation between the two parameters, and quantitative relations found using the correlation, such as that of
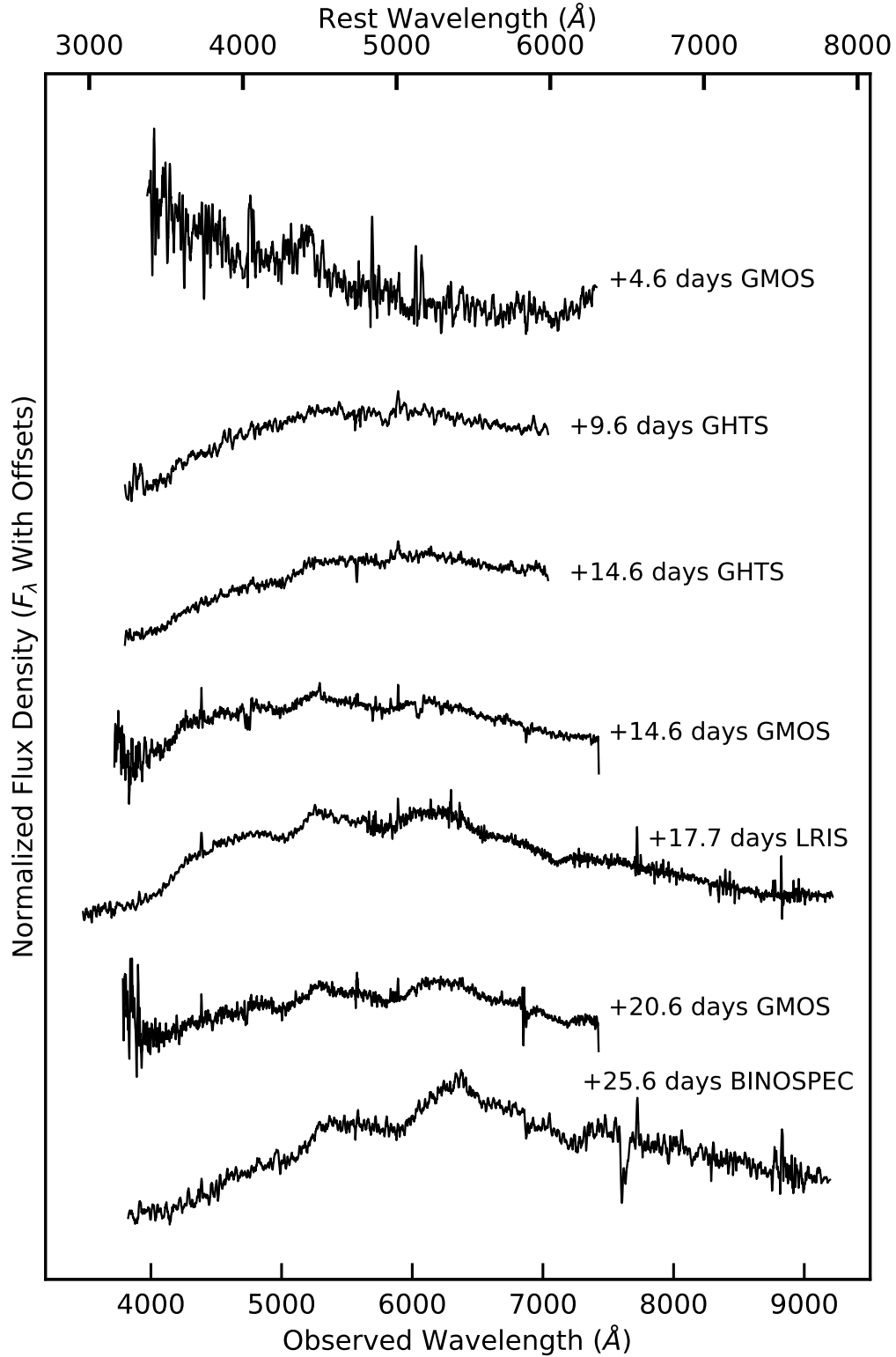
Figure 4. Optical spectra of SN 2025kg. The phases are relative to the time of the accompanying X-ray transient EP250108a's detection. The spectra start dominated by a blue underlying continuum, though broad features already are beginning to develop in the first epoch. The spectra redden with time and strongly resemble an SN Ic-BL.

M. D. Stritzinger et al. (2018), must be viewed conservatively. Therefore, following the methodology used in G. P. Srinivasaragavan et al. (2024a) in their sample of SNe Ic-BL, we compute a conservative upper limit on the amount of host-galaxy extinction for SN 2025kg utilizing this relation. We measure an EW of $EW_{Na\,I} = 0.38 \pm 0.13$, which corresponds to an upper limit on the host-galaxy extinction of $A_V^{host}[mag] < 0.47$. We note that Ó. Rodríguez et al. (2023) present a different relation between $EW_{Na\,I}$ and A_V^{host}, with $A_V^{host}[mag] = 0.02 + 0.73 \times EW_{Na\,I} \pm 0.29$.   Using   this
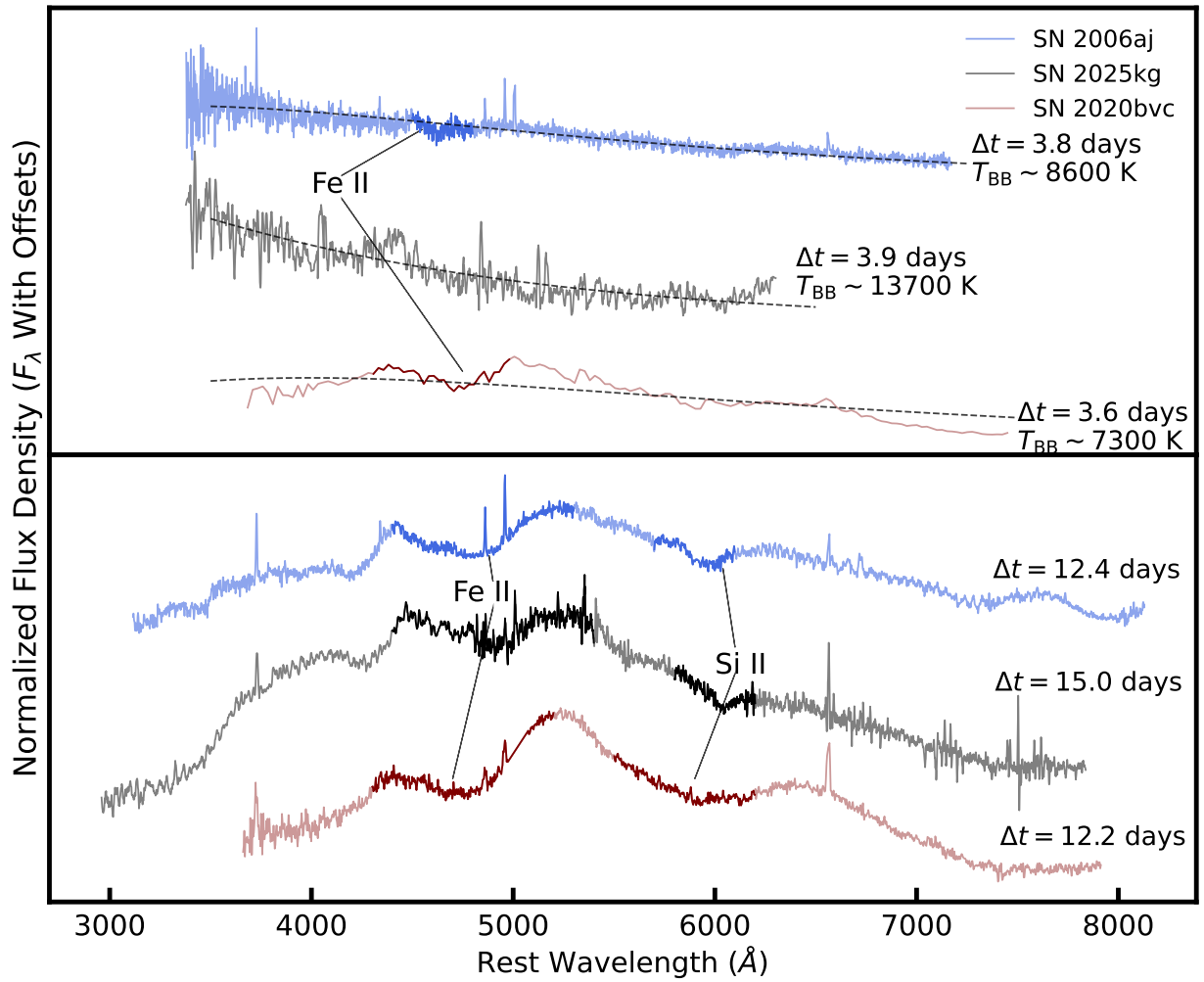
Figure 5. Spectra of SN 2025kg compared to spectra of SN 2006aj (M. Modjaz et al. 2006) and SN 2020bvc (A. Y. Q. Ho et al. 2020) at similar epochs, with times shown in the rest frame. Some host-galaxy lines are clipped for display purposes. The top panel shows the earliest spectrum we have of SN 2025kg along with comparison spectra, and we fit a blackbody to each spectrum to derive temperatures. We find that SN 2025kg has the highest temperature, and a possible broad Fe II feature is beginning to emerge in the spectrum (though we must interpret this with caution, and therefore we do not bold it in the figure; more in Section 3.3), and we also show blueshifted Fe II features in SN 2006aj's and SN 2020bvc's early-time spectra. The bottom panel shows a spectrum taken at the time of the peak of SN 2025kg in the r band, along with comparison spectra. We see clear blueshifted Fe II and Si II absorption features enabling an SN Ic-BL classification, labeled and shown in bold for SN 2025kg and for SN 2006aj and SN 2020bvc.

relation, we would derive A_V^{host} [mag] < 0.60. The difference between these two values is negligible, and we use the methodology from M. D. Stritzinger et al. (2018) to be consistent with the SN Ic-BL sample in G. P. Srinivasaragavan et al. (2024a).

We measure the velocity of the Fe II line at 5169 Å for each spectrum taken using the open-source code SESNspectraLib[31] (Y.-Q. Liu et al. 2016; M. Modjaz et al. 2016), which has been shown to be a good proxy for the photospheric expansion velocity v_{ph} (M. Modjaz et al. 2016). In order to do so, we first remove narrow galaxy emission lines and artifacts from bad pixels using the IRAF-based tool WOMBAT and then smooth the spectra using SESNspectraPCA.[32] SESNspectraLib calculates the blueshift of the Fe II line at 5169 Å relative to a standardized SN Ic spectroscopic template at the same phase. We estimate the uncertainty on the velocity by adding the uncertainty on the mean SN Ic template velocity in quadrature with the uncertainty on the relative blueshift. We note that the

---

Table 2
Photospheric Velocity Measurements of SN 2025kg

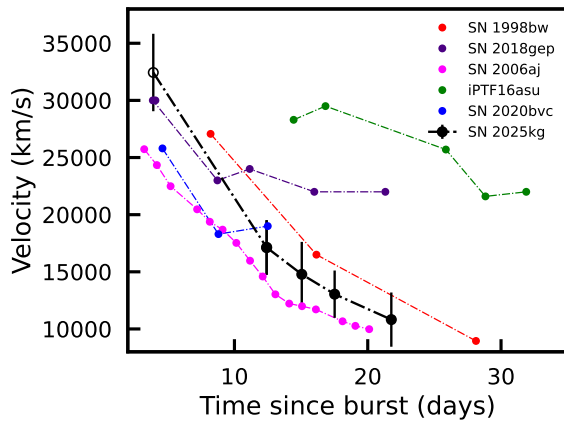| Time (days)	v_{ph} (km s^{-1})
4.6	$32,440 \pm 3388$[a]
14.6	$17,128 \pm 2389$
17.7	$14,779 \pm 2837$
20.6	$13,043 \pm 2069$
25.6	$10,816 \pm 2373$

Note.
[a] The first measurement must be treated with caution, due to the uncertainty of an Fe II feature in the first spectra (see Section 3.3 for details).

velocity derived for the first epoch at 4.6 days must be treated with caution, as the broad feature between 3800 and 4800 Å was not confirmed as being due to Fe II, as mentioned earlier.

In Figure 6, we compare v_{ph} for SN 2025kg to LLGRB 980425/SN 1998bw (K. Iwamoto et al. 1998), SN 2006aj (P. A. Mazzali et al. 2006), SN 2020bvc (A. Y. Q. Ho et al. 2020;

---

[31] https://github.com/metal-sn/SESNspectraLib
[32] https://github.com/metal-sn/SESNspectraPCA

Figure 6. Photospheric velocity evolution for SN 2025kg, compared to other prominent LLGRB SNe (SN 1998bw, K. Iwamoto et al. 1998; SN 2006aj, P. A. Mazzali et al. 2006) and other SNe Ic-BL that likely have different powering mechanisms than just radioactive decay (iPTF 16asu, L. Whitesides et al. 2017; SN 2018gep, A. Y. Q. Ho et al. 2019; SN 2020bvc, A. Y. Q. Ho et al. 2020), with times in the rest frame. SN 2025kg's $v_{\rm ph}$ evolves very similarly to SN 2006aj. The first measurement is shown with an open circle due to the uncertainty in the identification of an Fe II feature (see Section 3.3 for details).

L. Izzo et al. 2020; J. Rho et al. 2021), iPTF 16asu (L. Whitesides et al. 2017), and SN 2018gep (A. Y. Q. Ho et al. 2019; S.-C. Leung et al. 2021; T. A. Pritchard et al. 2021). We find that SN 2025kg's $v_{\rm ph}$ evolves very similarly to SN 1998bw and SN 2006aj, and its velocity is in between the two events. SN 2020bvc's $v_{\rm ph}$ is slower at early times but then flattens out and becomes consistent at around day 12. SN 2018gep's $v_{\rm ph}$ is similar and shows a similar evolution at early times but then flattens out and is significantly faster than SN 2025kg at later epochs. There are no early-time constraints on iPTF 16asu's $v_{\rm ph}$, but it also is significantly faster than SN 2025kg at later times, along with possessing a flatter evolution.

3.4. Radio Analysis

Historically, the majority of SNe associated with GRBs have been SNe Ic-BL, similar to SN 2025kg (M. Modjaz et al. 2016; Z. Cano et al. 2017). Therefore, the association of a Ic-BL SN with EP 250108A may indicate that the initial X-ray activity of EP 250108A is actually an LLGRB or a GRB observed off-axis (R. Yamazaki et al. 2003; Y. Urata et al. 2015). Here, we use our radio observations to explore the possibility of a GRB progenitor for EP 250108A.

The VLA observations of EP 250108A allow us to place limits on the 10 GHz luminosity of $\lesssim 10^{28}\,{\rm erg\,s^{-1}\,Hz^{-1}}$ (assuming $z = 0.176$) at rest-frame times of $\sim$5.5–44.7 days (Figure 7). Our radio limits are $\sim$3 orders of magnitude lower than the radio luminosity of typical on-axis long GRBs (e.g., P. Chandra & D. A. Frail 2012), effectively ruling out a standard on-axis long GRB. Similarly, the radio emission observed following XRF 020903 is ruled out, as the radio luminosity of XRF 020903 is $\sim$2 orders of magnitude higher at a similar rest-frame time (A. M. Soderberg et al. 2004). The canonical LLGRB is LLGRB 980425/SN 1998bw (T. J. Galama et al. 1998). Our radio observations of EP 250108A are $\sim$2–7× deeper than the radio emission observed following LLGRB 980425/SN 1998bw, ruling out 1998bw-like emission (S. R. Kulkarni et al. 1998; E. Waxman et al. 1998). However, our limits cannot rule out fast-fading radio emission similar to the low-luminosity event LLGRB 060218/SN 2006aj (A. M. Soderberg et al. 2006)
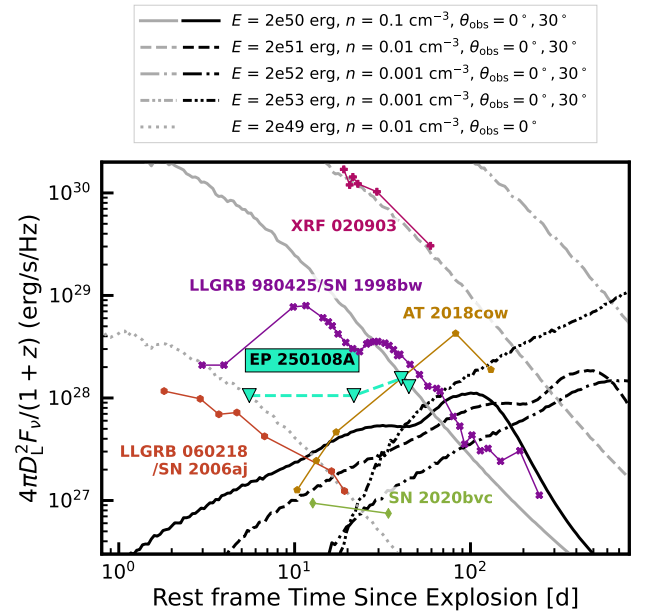
Figure 7. The 10 GHz radio light curve of our VLA nondetections of EP 250108A (green triangles). Also shown are the 8–12 GHz light curves of LLGRB 980425/SN 1998bw (purple; S. R. Kulkarni et al. 1998; E. Waxman et al. 1998), XRF 020903 (pink; A. M. Soderberg et al. 2004), LLGRB 060218/SN 2006aj (orange; A. M. Soderberg et al. 2006), SN 2020bvc (green; A. Y. Q. Ho et al. 2020), and AT 2018cow (yellow; R. Margutti et al. 2019). We additionally plot afterglow models for several pairs of total GRB jet energy (E) and circumburst density (n), generated with the FIREFLY code (R. G. Dastidar & P. C. Duffell 2024) for an on-axis ($\theta_{\rm obs} = 0^\circ$; gray) and off-axis ($\theta_{\rm obs} = 30^\circ$; black) jet. We cannot rule out radio emission similar to LLGRB 060218/SN 2006aj and SN 2020bvc.

or the nearby SN Ic-BL 2020bvc (A. Y. Q. Ho et al. 2020). Late-rising AT 2018cow–like emission is ruled out by our final VLA observation (R. Margutti et al. 2019).

Next, we explore whether EP 250108A could originate from an off-axis GRB, where the expectation is that the afterglow could become detectable at late times as the jet of the GRB decelerates and the beaming angle opens into our line of sight (e.g., D. Eichler & A. Levinson 1999; E. Nakar et al. 2002; H. van Eerten et al. 2010). Many searches for late-rising afterglows have been conducted following SNe Ic-BL, with no definitive off-axis candidates to date (e.g., E. Berger et al. 2003; A. M. Soderberg et al. 2006; A. Corsi et al. 2016, 2023), though an off-axis model was favored for SN 2020bvc by L. Izzo et al. (2020). We test whether our radio limits could be consistent with an off-axis afterglow by generating model light curves using the FIREFLY code (R. G. Dastidar & P. C. Duffell 2024). We set the power-law electron distribution to $p = 2.133$, the jet opening angle to $\theta_{\rm j} = 7^\circ$, and the energy imparted onto the electrons and magnetic field to $\epsilon_{\rm e} = 0.1$ and $\epsilon_{\rm B} = 0.01$ (similar to the values found for LGRBs; e.g., A. Panaitescu & P. Kumar 2002; S. A. Yost et al. 2003; S. B. Cenko et al. 2010, 2011; G. Ryan et al. 2015; T. Kangas & A. S. Fruchter 2021; G. Schroeder et al. 2022), and we vary the total energy of the GRB jet (E) and the circumburst density (n). We note that we assume a constant-density interstellar medium (ISM) environment—see R. A. J. Eyles-Ferris et al. (2025) for models presented in a wind-like medium. Though it may be expected that LGRBs occur in a stellar wind medium due to their massive star progenitors, multiple works show that a constant-density ISM environment approximation is able to model LGRB emission well in many cases (e.g.,

A. Panaitescu & P. Kumar 2002; S. Schulze et al. 2011;
B. P. Gompertz et al. 2018). Furthermore, C. M. Irwin &
K. Hotokezaka (2024) found that LLGRB 060218 was more
consistent with a constant-density ISM at a large radius than a
wind environment, and throughout this work, we find
similarities between EP250108a and LLGRB 060218.

We show a sample of allowed models for an off-axis
observing angle of $\theta_{obs} = 30°$ in Figure 7 compared to their
on-axis analogs ($\theta_{obs} = 0°$). Overall, our nondetections require
either a low circumburst density environment ($\lesssim 6 \times 10^{-3} \, cm^{-3}$) for a canonical $\sim 10^{52}$ erg GRB viewed $\gtrsim 30°$
off-axis, a low-energy GRB ($\lesssim 10^{50}$ erg) for a moderate
circumburst density environment ($\sim 10^{-1} \, cm^{-3}$) viewed
$\gtrsim 30°$ off-axis, or a highly offset jet for a canonical GRB
($E \sim 10^{52}$ erg and $n \sim 1 \, cm^{-3}$) viewed $\gtrsim 60°$ off-axis. The off-
axis models typically peak $\sim 10^2$–10^3 days (rest frame) after
the GRB; therefore, continued radio monitoring should be
performed to search for any late-rising emission.

In addition to some of the off-axis models, we also show the
model of an on-axis, extremely low-energy GRB similar to
LLGRB 060218 ($E \sim 5 \times 10^{49}$ erg; P. Ferrero et al. 2006),
with $E \sim 10^{50}$ in a moderate circumburst density environment
($n \sim 10^{-1} \, cm^{-1}$). We find that the model fits just under
EP250108a's first radio nondetection and is consistent with the
rest of the radio nondetections. Therefore, an on-axis,
extremely subenergetic jet is consistent with the radio
observations. This is consistent with the conclusions from
R. A. J. Eyles-Ferris et al. (2025), and we discuss this more in
Section 4.

3.5. X-Ray Analysis

The prompt X-ray emission of EP250108A detected by EP's
WXT in combination with its lack of associated γ-ray emission
further shows its possible association with LLGRBs and
XRFs. LLGRB 060218/SN 2006aj's peak X-ray luminosity
was $\sim 2.8 \times 10^{46} \, erg \, s^{-1}$. Though it peaked at 4.9 keV
(S. Campana et al. 2006), which is outside EP's WXT spectral
range, this is very similar to the peak X-ray luminosity
reported in Section 2.1 of $\sim 1.3 \times 10^{46} \, erg \, s^{-1}$. Furthermore,
the timescale for the prompt emission is similar, as LLGRB
060218 had prompt emission that lasted 2100 s (S. Campana
et al. 2006), which is the same as the rest-frame timescale of
EP250108a's prompt emission.

Follow-up X-ray observations (described in Section 2.1) of
EP250108A did not detect any emission in the 0.3–10 keV
bands. In Figure 8, we place the X-ray upper limits of
EP250108a in the context of other X-ray transients. The upper
limits rule out emission as bright as classical GRB 230812B/
SN 2023pel (T. Hussenot-Desenonges et al. 2024; G. P. Srini-
vasaragavan et al. 2024b), which we show as a comparison to
demonstrate how underluminous the rest of the transients
shown in the figure are in X-rays to classical GRBs. We are
not able to rule out emission similar to AT 2018cow
(L. E. Rivera Sandoval et al. 2018), LLGRB 060218a/SN
2006aj (S. Campana et al. 2006), LLGRB 980425/SN 1998bw
(C. Kouveliotou et al. 2004), and SN 2020bvc (A. Y. Q. Ho
et al. 2020).

4. Light-curve Modeling

There have been numerous stripped-envelope SNe of
varying types that display double peaks in their light curves.
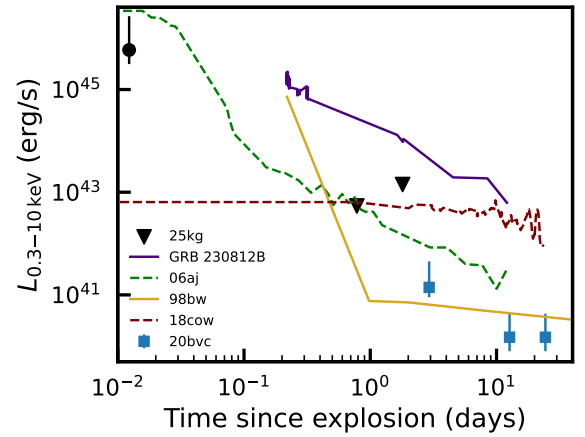
Figure 8. Comparison of 0.3–10 keV X-ray upper limits of EP250108a/SN 2025kg to the X-ray light curves of GRB 230812B/SN 2023pel (T. Hussen-ot-Desenonges et al. 2024; G. P. Srinivasaragavan et al. 2024b), LLGRB 060218a/SN 2006aj (S. Campana et al. 2006), LLGRB 980425/SN 1998bw (C. Kouveliotou et al. 2004), double-peaked SN Ic-BL SN 2020bvc (A. Y. Q. Ho et al. 2020), and LFBOT AT 2018cow (L. E. Rivera Sandoval et al. 2018), with times in the rest frame. The WXT detection is also shown, though we show the luminosity in the 0.5–4 keV range. We cannot rule out X-ray emission similar to SN 2006aj or SN 2020bvc.

The radioactive decay of ^{56}Ni (W. D. Arnett 1982) produces
the second peak in nearly all of these systems and drives the
majority of SN emission during the photospheric phase.

However, the origin of the first peak is not as certain. SCE
(E. K. Grasberg & D. K. Nadezhin 1976; S. W. Falk &
W. D. Arnett 1977; R. A. Chevalier 1992; E. Nakar &
R. Sari 2010; A. L. Piro et al. 2010; I. Rabinak &
E. Waxman 2011; K. K. Das et al. 2024) from SN ejecta
interacting with an extended CSM is one possible explanation.
In this scenario, the progenitor star has a compact core and a
low-mass extended shell M_e, which extends out to a radius R_e
(A. L. Piro et al. 2010; M. C. Bersten et al. 2012; E. Nakar &
A. L. Piro 2014; but see N. Sapir & E. Waxman 2017 for an
alternative interpretation). After the initial SBO from the
surface of the progenitor explodes through the outer, low-mass
shell (which lasts on a timescale of hours), this material
eventually expands and cools over the following days,
producing a luminous, blue first peak. Unlike in Type IIb
SNe, where M_e is thought to be the outer stellar envelope of
the progenitor star, M_e in SNe Ic-BL is theorized to be from
material ejected in mass-loss episodes, perhaps due to binary
interactions (R. A. Chevalier 2012), or stellar winds
(E. Quataert & J. Shiode 2012).

The presence of prompt X-ray emission and the similarities
to LLGRB 060218/SN 2006aj across different wavelengths
motivate the testing of collapsar jet-driven models to explain
the first peak. The blue peak contrasts with the expected
nonthermal emission of classical GRBs but can be explained
by the cooling of a shocked cocoon (E. Nakar & T. Piran 2017;
A. L. Piro & J. A. Kollmeier 2018). In this model, the GRB jet
creates a cocoon as it propagates through the stellar
atmosphere and imparts a significant amount of energy
(10^{51}–10^{52} erg) into it. This cocoon radiates as it expands
and cools within the stellar envelope, generating thermal
emission. Another possible scenario is the interaction of this
cocoon with an extended CSM, where emission is generated
from cooling with the surrounding CSM (E. Nakar 2015).

In this section, we present modeling of the optical LC,
where we first fit the second peak of the LC beginning at

$T_0 + 8$ days to the radioactive decay model in order to derive the SN explosion parameters. We then simultaneously fit the first peak and second peak to a combined radioactive decay model with each of the three models presented above. Hereafter, these scenarios are referred to as follows.

(a) *SN ejecta–CSM*. Emission is generated from interaction of the SN ejecta with an extended CSM (A. L. Piro et al. 2021).

(b) *Collapsar jet-driven shocked cocoon*. Emission is powered by emission from the cocoon of a collapsar-powered jet choked in its stellar envelope (E. Nakar & T. Piran 2017; A. L. Piro & J. A. Kollmeier 2018).

(c) *Collapsar jet-driven shocked cocoon–CSM*. Emission is powered by emission from the cocoon of a collapsar-powered jet choked with an extended CSM (E. Nakar 2015).

The fitting of the second peak of the LC independent of the first peak is justified, as any contributions from shock cooling or jet-driven models will be negligible during these time periods. This is also the treatment used in J. C. Rastinejad et al. (2025). However, in order to derive the parameters of the first peak accurately, we believe a combined treatment of the radioactive decay model and a model describing the first peak is necessary. This is because the photometry between days 4 and 7 likely has contributions from both models during the transition from the end of the first peak to the beginning of the radioactive decay peak. This differs from the treatment in R. A. J. Eyles-Ferris et al. (2025) and is likely a major reason for some discrepancies in the parameters derived.

Below, we present descriptions of each of the models. We perform the fits for all the models through their implementations in REDBACK (N. Sarin et al. 2024), an open-source electromagnetic transient Bayesian inference software (N. Sarin et al. 2024). In order to derive posteriors and perform the sampling, we utilize bilby (G. Ashton et al. 2019) and Dynesty (J. S. Speagle 2020). We perform the radioactive decay fit to the bolometric luminosity LC while performing the fits of models (a), (b), and (c) combined with the radioactive decay model on the photometry. We fit the bolometric luminosity LC to derive the SN explosion parameters for consistency with the literature, as most SNe Ic-BL have their parameters derived through fitting the W. D. Arnett (1982) model to their bolometric luminosity LCs (F. Taddia et al. 2019; G. P. Srinivasaragavan et al. 2024a). Furthermore, the BC coefficients used to derive the bolometric luminosity LC (J. D. Lyman et al. 2014) are well defined for stripped-envelope SNe in the radioactive decay phase.

However, these BC coefficients are not as well defined for stripped-envelope SNe in the shock cooling phase (described in Section 3.2), so there are likely significant systematic uncertainties that would dominate fitting the bolometric light curve first peak with our models. Furthermore, R. A. J. Eyles-Ferris et al. (2025) fit the first peak using photometry, so this allows for consistent comparisons between our work. Similarly to R. A. J. Eyles-Ferris et al. (2025), we fit the models assuming a Gaussian likelihood with a systematic error added in quadrature to the statistical errors on the photometry, σ_{sys}, to capture systematic uncertainties in the photometry, as well as the priors used. R. A. J. Eyles-Ferris et al. (2025) set this error equivalent to 0.15, but we let it vary as a free parameter in our fits. We also allow the host-galaxy extinction A_V to vary in our

Table 3
Explosion Properties of SN 2025kg's Radioactive Decay (Second) Peak from LC Modeling

Parameter	Median
M_{Ni} ($M_\odot$)	$0.57^{+0.60}_{-0.30}$
E_{KE} (10^{51} erg)	$2.91^{+1.36}_{-0.86}$
M_{ej} ($M_\odot$)	$1.66^{+0.79}_{-0.49}$

photometry fits as a free parameter, with a prior between 0 and 0.47 mag (the upper limit we found in Section 3.3).

4.1. Radioactive Decay Model

First, we describe the W. D. Arnett (1982) model that we use to fit the second peak as well as utilize in combination with cases (a), (b), and (c) to derive the first peak's parameters. The radioactive decay model of W. D. Arnett (1982) assumes that the instantaneous heating rate from the decay of ^{56}Ni and ^{56}Co equals the peak bolometric luminosity of the SN. This model assumes spherical symmetry and further radioactive inputs (S. Valenti et al. 2008). We do not assume full γ-ray trapping and account for γ-ray leakage in the late-time LC (A. Clocchiatti & J. C. Wheeler 1997). The model's main free parameters are the nickel mass (M_{Ni}) and characteristic photon diffusion timescale (τ_m), where M_{Ni} sets the peak of the bolometric light curve and τ_m is a proxy for the rise time of the SN and relates to the kinetic energy (E_{KE}) and ejecta mass (M_{ej}) of the SN through

$$M_{ej} = \frac{\tau_m^2 \beta c v_{sc}}{2\kappa_{opt}} \quad (4)$$

and

$$E_{KE} = \frac{3v_{sc}^2 M_{ej}}{10}, \quad (5)$$

where $\beta = 13.8$ (S. Valenti et al. 2008), c is the speed of light, κ_{opt} is a constant average optical opacity, and v_{sc} is the photospheric velocity v_{ph} at peak light. In our fitting procedure, the free parameters we use are M_{ej}; the fraction of nickel in the ejecta f_{Ni}; v_{ej}, which is a representative of the initial ejecta velocity; κ_{opt}; the γ-ray opacity κ_γ; and the temperature where the photosphere begins to recede, T_{floor}. All of these parameters have broad, uninformed priors in the fitting. These are the same parameters used in the one-zone model used in J. C. Rastinejad et al. (2025), who fit their photometry, except we do not include the host-galaxy extinction, A_V. We do not include this in our fitting procedure, as REDBACK cannot incorporate extinction into its luminosity fits. However, this is justified, as we showed in Section 3.3 that the host extinction is minimal. We note that J. C. Rastinejad et al. (2025) also test a nickel mixing model (Sarin 2025, in preparation) and find significant evidence of mixing, where M_{Ni} is distributed into ~60% of the outer mass layers. We do not test this model, as we do not have sufficient late-time, multiband photometry to get good constraints on the amount of nickel mixing present.

We report the 1D marginalized posterior median and 68% credible interval of the major parameters in Table 3. We derive $M_{Ni} \sim 0.6\ M_\odot$ and $M_{ej} \sim 1.7\ M_\odot$. Using the photospheric velocity derived in Section 3.3 of ~17,000 km s^{-1} around peak

light, we derive $E_{KE} \sim 2.8 \times 10^{51}$ erg. All values that we derive are consistent with those found in J. C. Rastinejad et al. (2025) from their one-zone modeling, and the ejecta mass and kinetic energy are consistent with the overall SN Ic-BL population (F. Taddia et al. 2019; G. P. Srinivasaragavan et al. 2024a). The nickel mass is slightly outside the 1σ range of F. Taddia et al. (2019), but the range they report is for "ordinary" SNe Ic-BL after removing two outlier events from their sample (iPTF 15eov and iPTF 16asu). When including these two events, the nickel mass is consistent with their median and is also consistent with the sample from G. P. Srinivasaragavan et al. (2024a), who do not remove any events when calculating median values.

The nickel mass we derive is significantly higher than that of SN 2006aj ($M_{Ni} = 0.2 \pm 0.1 \, M_\odot$; Z. Cano et al. 2017) and SN 2020bvc ($M_{Ni} = 0.4 \, M_\odot$; J. Rho et al. 2021) but similar to SN 1998bw ($M_{Ni} = 0.3-0.9 \, M_\odot$; J. Sollerman et al. 2000). This is consistent with the relative brightness of each of these events, as SN 2025kg possesses a significantly higher peak absolute magnitude than SN 2006aj and SN 2020bvc and a similar peak magnitude to SN 1998bw. We note that the true nickel mass is likely lower than the value we derive, as J. C. Rastinejad et al. (2025) find significant evidence of nickel mixing throughout the outer ejecta, but we do not test this model.

4.2. Model (a): SN Ejecta–CSM

We fit individual band LCs to a combination of the SCE model from A. L. Piro et al. (2021) and radioactive decay model from W. D. Arnett (1982). Here we summarize the major equations needed to describe model (a). The SCE luminosity is described as

$$L(t) \approx \frac{\pi(n-1)}{3(n-5)} \frac{cR_e v_t^2}{\kappa} \left(\frac{t_d}{t}\right)^{4/(n-2)}, \quad t \leqslant t_d. \quad (6)$$

and

$$L(t) = \frac{\pi(n-1)}{3(n-5)} \frac{cR_e v_t^2}{\kappa} \exp\left[-\frac{1}{2}\left(\frac{t^2}{t_d^2} - 1\right)\right], \quad t \geqslant t_d, \quad (7)$$

where t_d is the time where the diffusion reaches a characteristic velocity v_t of the shock, or

$$t_d = \left[\frac{3\kappa K M_e}{(n-1)v_t c}\right]^{1/2}. \quad (8)$$

n is a power-law index that describes the density of the outer region of the ejecta with respect to radius, and its typical value is $n \approx 10$. Similarly, δ is a power-law index that describes the density of the inner region of the ejecta with respect to radius, and its typical value is $\delta \approx 1.1$. K is a constant set by mass conservation, represented as

$$K = \frac{(n-3)(3-\delta)}{4\pi(n-\delta)}. \quad (9)$$

For typical values, $K = 0.119$. M_e is the mass of the extended envelope, R_e is the radius of the envelope, and κ is a constant opacity. We fit a combination of the W. D. Arnett (1982) model and model (a) to SN 2025kg's photometry, where the major free parameters for model (a) are M_e, R_e, and E_e (the energy in the envelope), all with broad, uninformed priors. As
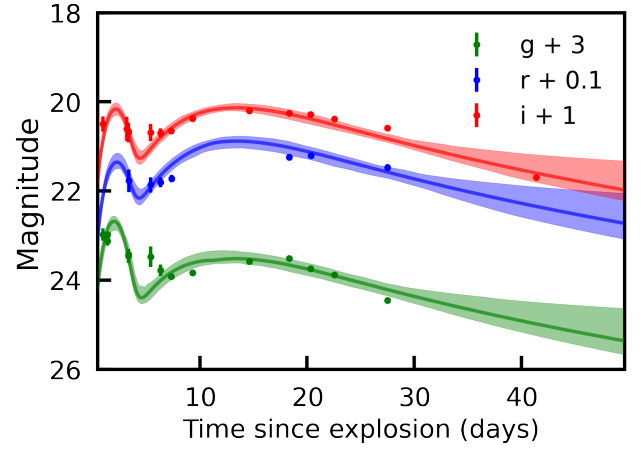
Figure 9. Fitting of model (a) (SN ejecta–CSM) and the radioactive decay model of W. D. Arnett (1982) in combination with the photometry of SN 2025kg. We show the maximum-likelihood fit and the 90% credible interval.

Table 4
Properties of Model (a) for SN 2025kg (First Peak) from LC Modeling

Parameter	Median
M_e ($M_\odot$)	0.04 ± 0.01
R_e (10^{13} cm)	$34.67^{+31.40}_{-17.30}$
E_e (10^{51} erg)	$0.23^{+0.27}_{-0.13}$

we are fitting the two models simultaneously, we also invoke a condition between E_e and E_{KE}, presented in A. L. Piro et al. (2021), where only a fraction of the total energy of the SN is allowed to be injected into the extended envelope,

$$E_e \approx 2 \times 10^{49} E_{51} \left(\frac{M_c}{3 \, M_\odot}\right)^{-0.7} \left(\frac{M_e}{0.01 \, M_\odot}\right)^{0.7}, \quad (10)$$

where E_{51} is $E_{KE}/10^{51}$ (which we fix to the value derived in Section 4.1) and M_c is the mass of the helium core, which is $\sim M_{ej}$.

We show the results of the fitting for the major parameters in Table 4, where we report the 1D marginalized posterior median and 68% credible interval. In Figure 9, we show the maximum-likelihood estimate of the joint fit to the photometry, along with the 90% credible interval of the posteriors on the joint fit. We find $M_e \sim 0.04 \, M_\odot$, $R_e \sim 3.5 \times 10^{14}$ cm, and $E_e \sim 2.3 \times 10^{50}$ erg and that this model can describe the optical LC well.

The parameters we derive are significantly different than those derived in R. A. J. Eyles-Ferris et al. (2025). They also test the A. L. Piro et al. (2021) model and find $M_e > 6 \, M_\odot$ and $E_e > 10^{52}$ erg for the A. L. Piro et al. (2021) model, which are inconsistent with our results. We believe the large discrepancy is due to the difference in fitting methods—we account for contributions from the radioactive decay component during the first 6 days, while R. A. J. Eyles-Ferris et al. (2025) do not. Therefore, we believe this leads them to derive larger parameters than needed when including the contribution from radioactive decay, particularly during days 4–6 after T_0. It also may be due to the difference in treatment of the systematic error σ_{sys}, which we allowed to vary in our fits. They also test a dense CSM model with an abrupt drop in density

Table 5
Properties of Model (b) for SN 2025kg from LC Modeling

Parameter	Median
M_{cocoon} ($M_\odot$)	$1.19^{+0.49}_{-0.46}$
$v_{\text{cocoon}}(c)$	$0.08^{+0.02}_{-0.02}$
f_{shocked}	$0.63^{+0.16}_{-0.17}$
t_{shocked} (s)	$63.88^{+22.60}_{-20.16}$
θ_{cocoon}	$19°.95 \pm 5°.89$

(B. Margalit 2022) and find that these parameters are more consistent with the expected emission. However, we do not invoke this model, as the treatment of A. L. Piro et al. (2021) provided reasonable parameters.

4.3. Model (b): Collapsar Jet-driven Shocked Cocoon

Next, we fit a shocked cocoon model following E. Nakar & T. Piran (2017) and A. L. Piro & J. A. Kollmeier (2018), in addition to the W. D. Arnett (1982) radioactive decay model. In this model, the GRB jet propagates through the stellar atmosphere, which possesses a mass profile

$$m(>v) = M \left(\frac{v}{v_0} \right)^{(-\eta+1)}, \quad (11)$$

where M is the total ejecta mass, v_0 is the minimum velocity of the ejecta, and η is a power-law index, and the profile extends out to a radius R in centimeters. There are two components to the shocked cocoon here—an inner shocked jet cocoon that produces high-energy emission and an outer stellar shocked cocoon, whose cooling emission produces optical emission (see Figure 1 in E. Nakar & T. Piran 2017 for a schematic of this model). Here, we model the emission from the shocked stellar cocoon. The luminosity an observer sees originates from the optical depth where the diffusion time (t_{diff}) is equal to the observation time, and the energy at that depth goes as $E \propto \frac{MvR}{t}$, along with the corresponding luminosity, $L(t) \sim E(t)/t_{\text{diff}}$ (see E. Nakar & T. Piran 2017; A. L. Piro & J. A. Kollmeier 2018 for full detailed equations). In our modeling, we assume that the shocked ejecta is confined within θ_{cocoon}. The additional major free parameters in the fitting, which we fit in conjunction to the radioactive decay model, are the mass of the cocoon M_{cocoon}, its velocity v_{cocoon}, η, the time the shock lasts t_{shock}, and the fraction of the ejecta mass that is in the shocked cocoon f_{shocked}. To derive the true mass of the shocked ejecta, we must correct for the geometry of the cocoon, so $M_{\text{shocked}} \sim \frac{f_{\text{shocked}} M_{\text{cocoon}} \theta^2}{2}$ (A. L. Piro & J. A. Kollmeier 2018). We note that for the optical emission, we are modeling the cooling emission from the stellar shocked cocoon.

We report the 1D marginalized posterior median and 68% credible interval of the major parameters in Table 5. In Figure 10, we show the maximum-likelihood estimate of the joint fit to the photometry, along with the 90% credible interval of the posteriors on the joint fit. We find that the mass of the shocked ejecta is $\sim 0.05\,M_\odot$; it is confined within $\sim 20°$ in a shock radius of $\sim 2\,R_\odot$ cm, resulting in a kinetic energy of $\sim 4 \times 10^{50}$ erg; and this model can describe the optical LC well. Our parameters are overall consistent with what
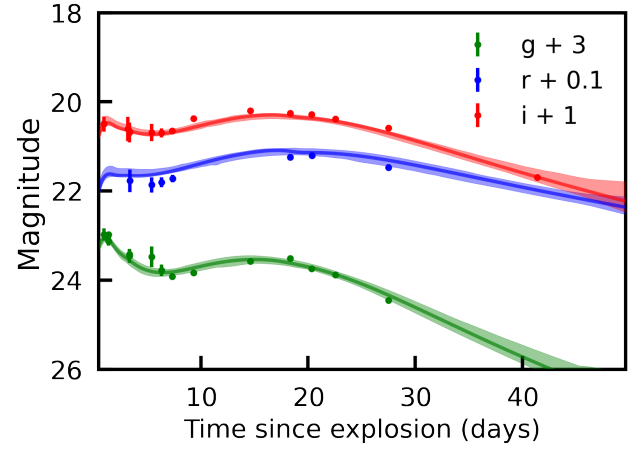
Figure 10. Fitting of model (b) (collapsar jet-driven shocked cocoon) and the radioactive decay model of W. D. Arnett (1982) in combination with the photometry of SN 2025kg. We show the maximum-likelihood fit and the 90% credible interval.

R. A. J. Eyles-Ferris et al. (2025) found fitting the same model, though on the lower end of what they derived.

4.4. Model (c): Collapsar Jet-driven Shocked Cocoon–CSM

We then fit a model in which the GRB progenitor (a stripped-envelope Wolf–Rayet star) is surrounded by an extended CSM (E. Nakar 2015), generated via mass loss prior to core collapse, in addition to the W. D. Arnett (1982) radioactive decay model. This scenario is motivated by growing observational evidence for extended CSM around stripped-envelope core-collapse SNe (e.g., R. J. Foley et al. 2007; A. Pastorello et al. 2007, 2008; C. Pellegrino et al. 2024), and the striking similarity between EP250108a and the LLGRB 060218, which has been interpreted as a failed GRB jet in an extended CSM (E. Nakar 2015). We thus consider a GRB jet launched from the stellar core that propagates through the extended CSM, producing a hot cocoon that emits cooling radiation.

We solve the jet propagation through the CSM and derive the resulting jet cocoon properties as a function of the CSM mass (M_{CSM}), radius (R_{CSM}), and central engine energy (E_{eng}). We assume a wind-like CSM density profile, $\rho \propto r^{-2}$, corresponding to constant mass loss. The central engine is modeled with a constant jet power ($=E_{\text{eng}}/t_{\text{eng}}$) over $t_{\text{eng}} \sim 100$ s, comparable to the progenitor's freefall timescale (C. D. Matzner 2003). A typical LGRB jet opening angle of $10°$ is adopted. The jet cocoon dynamics are modeled analytically (O. Bromberg et al. 2011; R. Harrison et al. 2018; H. Hamidani & K. Ioka 2021, 2023a; H. Hamidani et al. 2025a), yielding the breakout time and the cocoon's mass and energy. Postbreakout, the cocoon expands homologously, with a velocity structure set by mass and energy conservation. We adopt $dE_{\text{c}}/d\log(\Gamma\beta) \sim$ const. (E. Nakar & T. Piran 2017; M. Eisenberg et al. 2022), resulting in a density profile $\rho \propto v^{-5} t^{-3}$ (A. Suzuki et al. 2024), and internal energy evolution $E_{\text{c,i}} \propto t^{-1}$ due to adiabatic cooling.

Thermal photons escape via diffusion, with emission originating near the shell where $\tau \sim c/(v_{\text{out}} - v)$ (S. Kisaka et al. 2015; H. Hamidani & K. Ioka 2023b). The bolometric luminosity is computed from the inward motion (in Lagrangian coordinates) of this diffusion front, and the effective
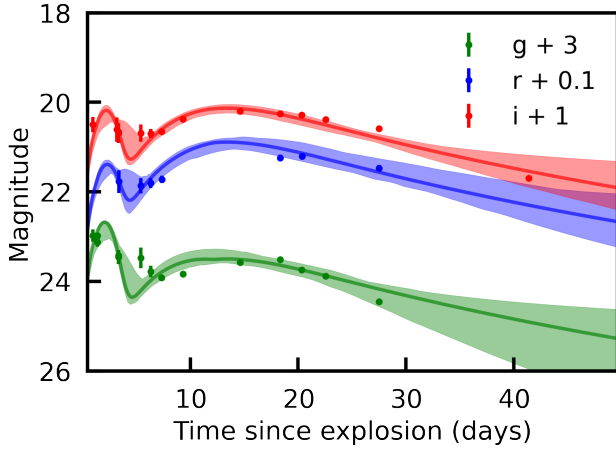
Figure 11. Fitting of model (c) (collapsar jet-driven shocked cocoon in extended CSM) and the radioactive decay model of W. D. Arnett (1982) in combination with the photometry of SN 2025kg. We show the maximum-likelihood fit and the 90% credible interval.

Table 6
Properties of Model (c) for SN 2025kg from LC Modeling

Parameter	Median
M_{CSM} ($M_\odot$)	$0.07^{+0.06}_{-0.04}$
R_{CSM} (10^{13} cm)	$3.71^{+8.58}_{-2.13}$
E_{eng} (10^{51} erg)	$5.75^{+20.00}_{-4.96}$

temperature is derived using the Stefan–Boltzmann law, assuming gray opacity $\kappa \sim 0.1$–$0.2\,\mathrm{cm^2\,g^{-1}}$, consistent with Thomson scattering.

We report the 1D marginalized posterior median and 68% credible interval of the major parameters in Table 6. In Figure 11, we show the maximum-likelihood estimate of the joint fit to the photometry, along with the 90% credible interval of the posteriors on the joint fit. We find $M_{CSM} \sim 0.1\,M_\odot$, $R_{CSM} \sim 4 \times 10^{13}$ cm, and $E_{eng} \sim 6 \times 10^{51}$ erg and that this model can describe the optical LC well. R. A. J. Eyles-Ferris et al. (2025) do not test this model, so we cannot make any comparisons.

5. Expected X-Ray Emission

In Section 4, we found that all three models can describe the optical LC well when combined with a radioactive decay model. Here we compare the expected X-ray emission from models (a), (b), and (c) in the WXT bandpass of 0.5–4 keV to the prompt emission detection described in Section 2.1.

5.1. Model (a): SN Ejecta–CSM

We use the same treatment as in A. Haynie & A. L. Piro (2021), who present an analytic method to calculate SBO emission in an extended CSM, followed by the calculation of the observed temperature from E. Waxman & B. Katz (2017).

Given the average 0.5–4 keV luminosity of $L_{X\text{-ray}} \sim 6 \times 10^{45}\,\mathrm{erg\,s^{-1}}$ and the prompt emission timescale of 2500 s, this corresponds to an energy of the SBO $E_{SBO} \sim 1.5 \times 10^{49}$ erg. The timescale of the breakout is dependent on whether the dominant rate-limiting process for the rise of the SBO is due to diffusion or to the light travel time. If the rise time of the SBO

luminosity set by diffusion is longer than the light travel time, then diffusion will dominate. The rise time is

$$t_r = \frac{R_e^2}{R_d v_t}, \tag{12}$$

where we use the median $R_e \sim 5 \times 10^{13}$ cm and $v_t \sim 0.2c$. R_d is

$$R_d = \frac{\kappa D v_t}{c}, \tag{13}$$

where κ is the opacity, and D is the mass loading factor,

$$D = \frac{\dot{M}}{4\pi v_t}. \tag{14}$$

Integrating this expression with respect to the mass, where we use $M_e \sim 4\pi R_e D$, and substituting into the expression for R_d, we get

$$R_d = \frac{\kappa v_t}{c} \frac{M_e}{4\pi R_e}. \tag{15}$$

Therefore, substituting this into the expression for t_r, we find

$$t_r = \frac{4\pi R_e^3 c}{\kappa M_e v_t^2}. \tag{16}$$

The light travel time t_l is simply $\frac{R_e}{c}$. Therefore, we have the inequality

$$\frac{4\pi R_e^3 c}{\kappa M_e v_t^2} > \frac{R_e}{c} \tag{17}$$

for diffusion to dominate. Rearranging, we derive

$$M_e < \frac{4\pi R_e^2}{\kappa} \left(\frac{c}{v_t}\right)^2. \tag{18}$$

Therefore, we find that the diffusion time only dominates if $M_e < 1.1\,M_\odot$, and we find $M_e \sim 0.04\,M_\odot$ from our modeling. Therefore, we are in the diffusion-dominated regime, and the luminosity of SBO in this scenario is

$$L_{SBO} = \frac{E_{SBO}}{t_r} \approx 4\pi D v_t^3, \tag{19}$$

which is $\sim 3 \times 10^{45}\,\mathrm{erg\,s^{-1}}$ for our parameters. This is less than the observed 0.5–4 keV X-ray luminosity of $\sim 10^{46}\,\mathrm{erg\,s^{-1}}$, even without accounting for the fact that only a fraction of this luminosity will go to 0.5–4 keV X-rays.

Furthermore, we compare t_r to the timescale of the prompt emission, as these two timescales should be approximately equal for model (a) to produce the prompt emission. Substituting known values into Equation (16), we find $t_r \sim 1$ day. This is much longer than the prompt emission timescale. Therefore, we find that though model (a) can reproduce the optical emission, it cannot reproduce the observed prompt X-ray emission, and we therefore disfavor this model in our analysis.

5.2. Model (b): Collapsar Jet-driven Shocked Cocoon

In Section 4.3, we focus on the thermal cooling emission from the shocked stellar cocoon that generates the optical emission. The shocked cocoon model we use is also expected

to produce high-energy X-ray and γ-ray emission through nonthermal emission mechanisms, primarily from the shocked jet component. However, the precise details of such emission are sensitive to uncertain assumptions such as the degree of mixing between the jet and stellar material and the mass/momentum profiles (e.g., E. Nakar & T. Piran 2017). Such calculations are beyond the scope of this work, but we use fiducial estimates in E. Nakar & T. Piran (2017) to compare to observations. Assuming no mixing, they find a γ-ray/hard X-ray signal that lasts on the order of seconds, with a spectrum peaking around 100 keV, which is inconsistent with the prompt detection from WXT.

We also compare the timescales between the optical emission and the prompt emission. In this case, the optical emission is highly independent of the X-ray emission, as the optical emission comes from the cooling of the stellar cocoon, and largely ignores the contributions from the shocked jet cocoon, which produces the X-rays. This is why the timescales for the two processes are very different—the shock-crossing timescale for the stellar cocoon is $\sim$63 s, while the prompt emission timescale is more than an order of magnitude larger.

In the X-ray regime, emission is possible if there is partial mixing, and the shocked jet cocoon energy is deposited in mildly relativistic material with $\Gamma < 10$. E. Nakar & T. Piran (2017) find that this emission would peak a day after the prompt burst, with a luminosity of $\sim 10^{44}$ erg s^{-1}. As the precise peak timescales and luminosities are sensitive to the various assumptions and different parameters, it is reasonable that this emission is consistent with the X-ray nondetections reported in Section 3.5. R. A. J. Eyles-Ferris et al. (2025) report that the parameters derived from this model in their analysis are consistent with the X-ray nondetections. However, the prompt X-ray emission is not obviously reproducible through model (b) for the fiducial choice of parameters and assumptions in E. Nakar & T. Piran (2017).

In order to describe the X-ray prompt emission, R. A. J. Eyles-Ferris et al. (2025) invoke a model somewhat independent of model (b) but consistent with the physical picture, utilizing models developed in Fryer et al. (2025, in preparation). In this model, bremsstrahlung emission arises from a failed jet propagating through the star or clumpy stellar wind, forming a semirelativistic cocoon. They find that this model can successfully explain the X-ray prompt emission. Therefore, it is possible that this model combined with model (b) can explain the X-ray prompt emission and first peak in the optical LC.

5.3. Model (c): Collapsar Jet-Driven Shocked Cocoon–CSM

As discussed in Section 4.4, a GRB jet propagating into an extended CSM can explain the observed early optical light curve. In this scenario, the extended CSM causes the jet to fail, forming a hot cocoon that expands through the surrounding material. The breakout of the cocoon from the CSM can also power X-ray emission via the SBO emission (e.g., E. Nakar 2015; E. Waxman & B. Katz 2017; C. M. Irwin & K. Hotokezaka 2024).

We estimate the X-ray luminosity using our median jet/CSM parameters that reproduce the optical light curve: $E_{\rm eng} \sim 6 \times 10^{51}$ erg, $R_{\rm CSM} \sim 4 \times 10^{13}$ cm, and $M_{\rm CSM} \sim 0.1$ $M_\odot$. We adopt an opacity of $\kappa \sim 0.1$ cm^2 g^{-1}.

The typical cocoon velocity can be found as $\bar{v} \sim \sqrt{2E_{\rm eng}/M_{\rm CSM}} \sim 0.25c$. This is a lower limit for the

SBO velocity. Considering that the outer part of the cocoon is slightly faster, we approximately take

$$v_{\rm SBO} \sim 0.3c. \tag{20}$$

The bolometric luminosity of the SBO is given by

$$L_{\rm SBO} \sim 4\pi R_{\rm CSM}^2 \rho_{\rm SBO} v_{\rm SBO}^3. \tag{21}$$

The optical depth gives $\tau \sim \kappa \rho_{\rm SBO} R_{\rm CSM} \sim c/v_{\rm SBO}$. Hence, the SBO luminosity can be found as

$$L_{\rm SBO} \sim 1.2 \times 10^{46} \text{ erg s}^{-1}, \tag{22}$$

and the observed timescale is set by the shock-crossing time as

$$t_{\rm obs} \sim 10^3 \text{ s}. \tag{23}$$

Both the total luminosity and observed timescale are broadly consistent with the observed prompt emission. However, only a fraction of the luminosity will be seen in the 0.5–4 keV bands, so here we calculate how much luminosity is generated in the observed frame of the prompt emission.

The effective temperature of the breakout emission given in E. Waxman & B. Katz (2017) is

$$T_{\rm eq} = 66 \rho_{-9}^{1/4} v_{t,9}^{1/2} \text{ eV}, \tag{24}$$

where ρ_{-9} is the density in terms of 10^{-9} g cm^{-3} and $v_{t,9}$ is v_t in terms of 10^9 km s^{-1}. Therefore, we find the effective temperature $T_{\rm eq} = 0.16$ keV.

However, this temperature only holds if the system is in true thermal equilibrium. In order to test this, we compute the thermal coupling coefficient in an expanding gas from E. Nakar & R. Sari (2010),

$$\eta \approx \frac{7 \cdot 10^5 \text{ s}}{\min\{t, t_d\}} \left(\frac{\rho}{10^{-10} \text{ g cm}^{-3}}\right)^{-2} \left(\frac{kT_{\rm eq}}{100 \text{ eV}}\right)^{7/2},$$

where k is the Boltzmann constant and $\min\{t_l, t_d\}$ is the minimum time between the light travel time and the diffusion time. Since we already determined that we are in the light travel regime, t_d is the minimum value. If $\eta < 1$, then the system is thermalized, and we can estimate the emission using the observed temperature $T = T_{\rm eq}$ as the blackbody temperature. However, if $\eta > 1$, then the spectrum transitions to an optically thin regime dominated by free–free emission, which is also modified by the Comptonization of these photons by the neighboring electrons (E. Nakar & R. Sari 2010). In this regime, the spectrum is a Wien spectrum at high energies, where the temperature is determined by

$$T\xi(T)^2 = T_{\rm eq}\eta^2, \tag{25}$$

where $\xi(T)$ is the Comptonization correction factor, given by

$$\xi(T) \approx \max\left\{1, \frac{1}{2}\ln[y_{\rm max}](1.6 + \ln[y_{\rm max}])\right\}, \tag{26}$$

where $y_{\rm max}$ is the Compton parameter,

$$y_{\rm max} \equiv \frac{kT}{h\nu_{\rm min}} = 3\left(\frac{\rho}{10^{-9} \text{ g cm}^3}\right)^{-1/2}\left(\frac{T}{100 \text{ eV}}\right)^{9/4}. \tag{27}$$

$y_{\rm max} < 1$ implies that Comptonization does not play a significant role, so $\xi = 1$, and $T = T_{\rm eq}\eta^2$. Therefore, we solve Equation (25) for T, substituting our known values, and, incorporating the fact that the density ρ will be a factor of 7

Table 7
CSM Parameters for SNe Ic-BL in the Literature

Event	M_e ($M_\odot$)	R_e (10^{13} cm)	Reference
EP250108a/SN 2025kg	$\sim$0.1	$\sim$3.7	This work
LLGRB 060218/SN 2006aj	$\sim$0.01 to $-$0.1	$\sim$4	C. M. Irwin & K. Hotokezaka (2024)
SN 2020bvc	$\sim$0.1	$\sim$10	J. Rho et al. (2021)
iPTF 16asu	$\sim$0.45	$\sim$0.17	L. Whitesides et al. (2017)
SN 2018gep	$\sim$0.3	$\sim$7.7	S.-C. Leung et al. (2021)
EP 240414a/SN 2024gsa	$\sim$0.33	$\sim$24	H. Sun et al. (2025)

larger due to the shock compressing the gas (E. Nakar & R. Sari 2010), we find $\eta = 70$. Then, solving Equation (25) to find the observed temperature, and we find $T = 1.2$ keV. Therefore, the majority of $L_{SBO} \sim 10^{46}$ erg s^{-1} will be seen in the 0.5–4 keV bands, which is consistent with the WXT prompt emission detection.

6. Discussion

Here we discuss the implications of our analysis and make inferences about the progenitor system of EP250108a/SN 2025kg. We focus our discussion on model (c), as we found that this model self-consistently reproduces both the X-ray prompt emission and first optical peak and therefore favor it in this work. We note that we do not rule out model (b), and we refer the reader to R. A. J. Eyles-Ferris et al. (2025) for more discussion on this model. There are additional models invoked to explain the emission in W. X. Li et al. (2025c), including an on-axis slow jet and a magnetar model to explain the SN emission, and we direct the reader to this work for more discussion on these models.

6.1. The Extended CSM Properties

Model (c) invokes an extended CSM, where cooling emission is generated from the interaction of the SN shock with the CSM. The invocation of an extended CSM is supported by detailed spectral analysis in J. C. Rastinejad et al. (2025), as they find evidence of a broadened Hα feature in an optical spectrum 42.5 days after T_0, as well as a He feature in a near-infrared spectrum taken near peak light. They conclude that the Hα feature is due to a detached hydrogen shell $\sim 10^{16}$ cm away from the progenitor, while the He feature is an indication of a helium shell of $<0.5\ M_\odot$, which they argue could be consistent with the dense CSM model invoked in R. A. J. Eyles-Ferris et al. (2025), at an extended radius $R_e \sim 7 \times 10^{14}$. Therefore, though the details of our modeling and results differ, our work agrees that an extended CSM is likely present in this system.

Now, we compare the extended CSM properties for SN 2025kg to other SNe Ic-BL that show evidence of having CSM interaction in the literature, and we show the masses and radii of the extended envelopes in Table 7. We include EP 240414a/SN 2024ga in the table, as H. Sun et al. (2025) model the second red peak at $M_r = -21$ mag, after the initial afterglow emission but prior to the SN's radioactive decay peak as SCE of dense, extended material at a large radius. We see that overall, the envelope masses in these systems range between 0.1 and 0.45 $M_\odot$, while the radii range from 1.7×10^{12} to 2.4×10^{14} cm. SN 2006aj has the most similar CSM parameters to SN 2025kg. However, SN 2025kg has a brighter initial peak, and the peak takes longer to decline

before transitioning to the radioactive decay component (see Section 3.1). This suggests a larger energy budget and larger envelope mass for SN 2025kg than SN 2006aj, which is supported by our modeling.

Though there is clear diversity in the observational properties of SNe Ic-BL that display SCE due to extended CSMs, understanding the landscape of the diversity of their progenitor systems is a complicated task. There are many degeneracies that exist between different parameters in these systems. The rise time and peak luminosity are dependent on the shock velocity and the radius of the extended envelope, while the shock velocity in turn is dependent on the density profile of the progenitor and the energy of the explosion, which in turn is dependent on the mass of the extended envelope. Therefore, it is difficult to pinpoint how important of a role each of these different parameters play in producing the range of observed SNe Ic-BL with extended CSM interaction.

The structure of the CSM surrounding SN Ic-BL progenitors is also likely diverse, determined by the origin of the mass-loss prior to the star's death, i.e., the presence of a binary, stellar outbursts, or winds (J. Fuller 2017; S. Wu & J. Fuller 2021). Different circumstellar material structures, especially asymmetric structures, can give rise to different SCE. In addition to the diversity of their progenitor systems, viewing angle effects may also play a role, as events viewed along their poles (SNe Ic-BL are expected to have asymmetric bipolar emission) will have brighter SCE than events viewed off-axis to these poles (A. Y. Q. Ho et al. 2020). Large sample studies of double-peaked SNe Ic-BL from a systematic perspective will be integral to understanding this landscape, and that will be the subject of a forthcoming paper (Vail et al., in preparation).

6.2. Understanding the X-Ray and Radio Emission

In Section 5, we determined that model (c) can self-consistently recreate the X-ray prompt emission. The inability of model (a) to reproduce the X-ray emission is consistent with what R. A. J. Eyles-Ferris et al. (2025) found in their work. Using a a convective engine model for the progenitor from Fryer et al. (2025, in preparation), where high-velocity ejecta is produced as the shock propagates out of the stellar edge, they found that they could only reproduce the X-ray observations in extreme cases, under the assumption that the SN energy exceeds current models, or we have an extreme mass and energy distribution with respect to the ejecta velocity (R. A. J. Eyles-Ferris et al. 2025). This method is different than the method we provide in Section 5, where we use an analytic calculation to compute the luminosity of SBO in an extended CSM. The fact that two independent methods arrive at the same conclusion, that model (a) cannot reproduce the X-ray prompt emission, gives further evidence that model (a) should be disfavored.

A collapsar-driven jet model is a more natural explanation for EP250108a/SN 2025kg, given its similarities to LLGRB 060218/ SN 2006aj, which is consistent with what R. A. J. Eyles-Ferris et al. (2025) found from their X-ray modeling of a collapsar jet-driven explosion. In model (c), we have a GRB jet that gets choked, depositing energy in a hot cocoon, and breaks out quasi-spherically and interacts with an extended CSM.

There are differing opinions on how dense of a CSM is needed to truly "choke" a jet—analytic works like H. Hamidani et al. (2025a) show that jets can fail from interacting with an extended CSM at radius $R_e > 10^{13}$, running into just $\sim 0.1\,M_\odot$ of material, and some simulations show that this holds true (A. Suzuki & K. Maeda 2022). If this is the case, this is a natural explanation for systems like LLGRB 060218/SN 2006aj. However, other simulations done by P. C. Duffell & A. Y. Q. Ho (2020) show that more than a few $M_\odot$ of material is necessary within 10^{13} cm to truly "choke" a jet. They found that with CSM parameters like those derived for SN 2006aj (as well as SN 2025kg), the CSM could not have fully choked the jet—it could just slow it down enough such that it spreads to a larger angle, but the SBO from the CSM would not be quasi-spherical as models suggest for SN 2006aj (e.g., E. Nakar 2015).

One way to reconcile these differences is to have a jet that is choked within its own stellar envelope that then goes on to interact with an extended CSM. If this were to occur, then we would still see a quasi-spherical SBO from the cocoon and shock cooling interaction with the extended CSM after the fact, where the emission is dependent on the CSM parameters, and the physics of E. Nakar's (2015) model we use in model (c) would still be accurate to describe the system. In order to have a jet choked at the stellar envelope (assuming a Wolf–Rayet progenitor, $R \sim 10^{12}$ cm), an intrinsically weak jet, short engine duration, or dense stellar envelope is necessary. R. A. J. Eyles-Ferris et al. (2025) argue that a failed jet through the stellar interior or a clumpy stellar wind can reproduce the prompt X-ray emission, which is similar to the above argument.

Both of these scenarios—where the jet is choked within its stellar envelope before interacting with an extended CSM or is choked by an extended CSM—are consistent with the radio nondetections. In Section 3.4, we showed that the only viable on-axis solution was a very energetically weak jet. It has been shown that the choking of the jet by the CSM leads to a weakening of the jet's energy (R. Margutti et al. 2015; E. Nakar 2015), and an intrinsic low-energy jet is also a natural explanation for why it may have been choked in its stellar envelope. Furthermore, model (c) is also consistent with the subsequent X-ray nondetections, as the X-ray emission duration is expected to match the shock-crossing timescale, lasting for $t_{\rm obs} \sim 10^3$ s (see Equation (23) in Section 5.3) before fading. This timescale is consistent with the later-time upper limits.

J. C. Rastinejad et al. (2025) argue that the He and Hα features detected in the spectra indicate the presence of at least a binary system, and maybe a tertiary system, where the helium shell was ejected in a common-envelope phase, while hydrogen was ejected either in a previous asymmetric common-envelope phase or through interactions with a third star. C. L. Fryer et al. (2025) argue that LGRBs arise from tight binary systems, and LLGRBs arise from wider binaries, with lower-mass BH-forming stars in the 20–30 $M_\odot$ range. If the He shell found in J. C. Rastinejad et al. (2025) is due to a

common-envelope phase, that necessitates a tight binary system. However, J. C. Rastinejad et al. (2025) also find that the zero-age main-sequence mass of the progenitor of SN 2025kg is between 19 and 30 $M_\odot$, if the central engine is a black hole. Lower-mass progenitors produce weaker jets (C. L. Fryer et al. 2025), and that gives an explanation of how the jet may have been choked in its stellar envelope, though the proximity of a nearby companion would be a competing effect.

Including EP250108a/SN 2025kg, EP has already found three SNe Ic-BL associated with FXTs (EP 240414a/SN 2024gsa, H. Sun et al. 2025; S. Srivastav et al. 2025; J. N. D. van Dalen et al. 2025; and EP 250304, L. Izzo et al. 2025) in its first year of operations. J. C. Rastinejad et al. (2025) report that the volumetric rates of such events are around $\sim$10–100 Gpc^{-3} yr^{-1}. This is significantly higher than the rates of classical, on-axis GRBs ($\sim$0.1–1 Gpc^{-3} yr^{-1}; e.g., M. Schmidt 2001; E. Liang et al. 2007; H. Sun et al. 2015), on the lower end of the rate of LLGRBs ($\sim$100–1000 Gpc^{-3} yr^{-1}; e.g., D. Guetta & M. Della Valle 2007; E. Liang et al. 2007; F. J. Virgili et al. 2009), and much lower than the rate of SNe Ic-BL ($\sim$1000 Gpc^{-3} yr^{-1}; W. Li et al. 2011; I. Shivvers et al. 2017). However, it is very similar to the rate of bursts detected by HETE-2, whose three onboard instruments operated from 2 to 400 keV (T. Sakamoto et al. 2005). A. Pélangeon et al. (2008) derive a rate of $\sim$10 Gpc^{-3} yr^{-1}, though they stress that this is a lower limit, as HETE-2 may have missed GRBs with peak energies less than 2 keV. They infer that the difference in their rate from those derived in other works that find $\sim$0.1–1 Gpc^{-3} yr^{-1} is the existence of XRFs in their sample.

Therefore, though there have only been a few events thus far, there is evidence that the SN Ic-BL population associated with FXTs is rarer than the normal SN Ic-BL population but less rare than classical LGRBs. Furthermore, their rates may be comparable to those of LLGRBS and are broadly consistent with the rate of GRBs detected by HETE-2, which included a significant number of XRFs. This points toward a possible similar progenitor system between SNe Ic-BL associated with EP FXTs, LLGRBs, and XRFs. However, the rate of EP FXTs derived by J. C. Rastinejad et al. (2025) is just an estimate, and a more robust calculation with more discovered events is necessary to draw any firm conclusions.

7. Conclusions

In this Letter, we present optical, X-ray, and radio observations of EP250108a/SN 2025kg, an SN Ic-BL associated with an FXT discovered by EP. Our main findings are as follows.

1. SN 2025kg possesses a double-peaked light curve. Its first peak is blue and has an absolute magnitude $M_g \sim -19.5$ mag, while the second peak has an absolute magnitude $M_r \sim -19.4$. Its light curve is very similar to LLGRB 060218/SN 2006aj, though both of its peaks are more luminous, while evolving on slower timescales.
2. SN 2025kg's spectral sequence transitions from a blue underlying continuum at early times with hints of broad absorption features to a redder continuum with multiple clear broad absorption features and a lack of H or He

features, characteristic of SNe Ic-BL. Its spectral evolution is very similar to that of SN 2006aj.

3. We analyze its X-ray prompt detection and subsequent X-ray and radio upper limits and determine that both radio and X-ray emission similar to LLGRB 060218A/SN 2006aj cannot be ruled out. We also find that the radio limits are consistent with various off-axis afterglow models, viewed at $\theta_{obs} \gtrsim 30°$. Future radio observations at $\sim$100–1000 days will constrain the presence of late-rising radio emission from a possible off-axis jet. We also find that an on-axis, very subenergetic GRB ($E \sim 10^{49}$ erg) in a moderate-density circumburst medium ($n \sim 10^{-1}$ cm^{-3}) is also consistent with the radio upper limits.

4. We model the second peak using the W. D. Arnett (1982) radioactive decay model to fit the bolometric luminosity light curve. We find that the SN parameters derived are overall consistent with the SN Ic-BL population.

5. We model the photometry with a combination of the W. D. Arnett (1982) radioactive decay model and three different models to describe the first peak. These are (a) SN ejecta interacting with an extended CSM, (b) the shocked cocoon of a collapsar jet choked in its stellar envelope, and (c) the shocked cocoon of a collapsar jet choked by an extended CSM. The three models can all reproduce the optical LC well.

6. We estimate the X-ray prompt emission generated in models (a), (b), and (c) and find that model (c) can reproduce the prompt emission detected by WXT self-consistently, and we therefore favor this model in this work. Model (b) is expected to produce high-energy X-ray emission; however, using the fiducial choice of parameters and assumptions from the model's paper (E. Nakar & T. Piran 2017), the prompt emission is not obviously reproducible. A combination of model (b) with another prompt emission model can explain EP250108a/SN 2025kg's properties well, and we do not rule it out (see R. A. J. Eyles-Ferris et al. 2025 for this interpretation).

7. In model (c), we find evidence that EP250108a/SN 2025kg possesses an extended CSM, with an envelope mass of $\sim$0.1 $M_{\odot}$ and a radius of $\sim$4 × 10^{13} cm. We place these parameters in the context of other SNe Ic-BL that show evidence of possessing an extended CSM and find that the parameters are most consistent with LLGRB 060218/SN 2006aj. The overall properties of EP250108a/SN 2025kg make it a close analog of LLGRB 060218/SN 2006aj.

Therefore, we conclude that EP250108a/SN 2025kg shows evidence of extended CSM interaction. EP has opened a new discovery space for discovering SNe Ic-BL in tandem with FXTs, providing a novel avenue for understanding their multiwavelength emission, as well as probing their surrounding CSM. Understanding the landscape of these unique SNe Ic-BL, along with their relation to LLGRBs, FXTs, XRFs, LFBOTs, and other known classes of relativistic transients, is essential for furthering our understanding of the continuum of relativistic stellar explosions and the various open questions that exist along that continuum.

Appendix

Here we provide a log of the spectroscopic and photometric observations, along with the corner plots associated with the LC modeling presented in Section 4, in Figures 12, 13, 14, and 15. We provide a log of the spectroscopic observations in Table 8, and the photometric observations in Table 9.
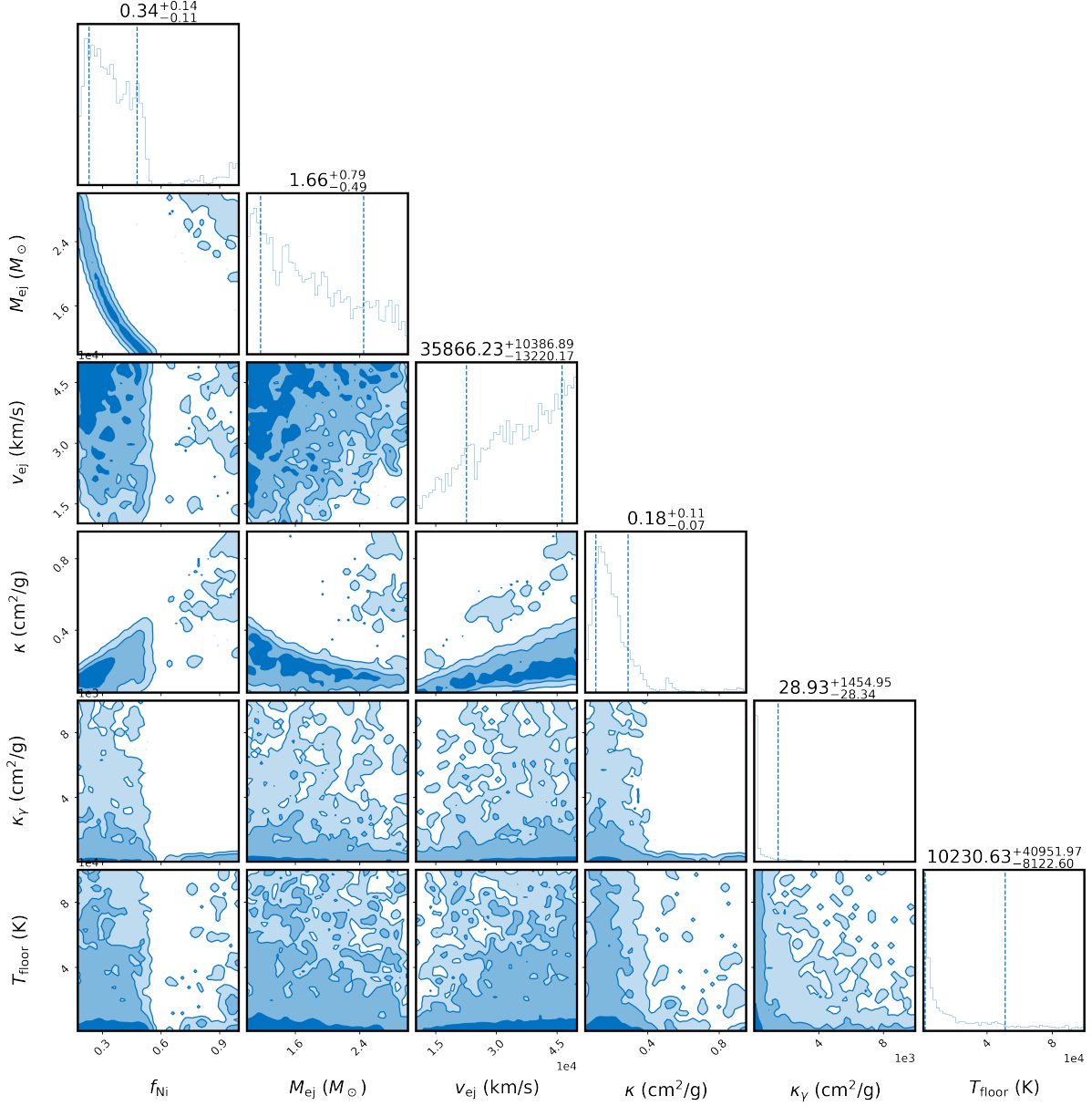
Figure 12. Corner plots associated with fitting the W. D. Arnett (1982) radioactive decay model to the bolometric luminosity LC's second peak.
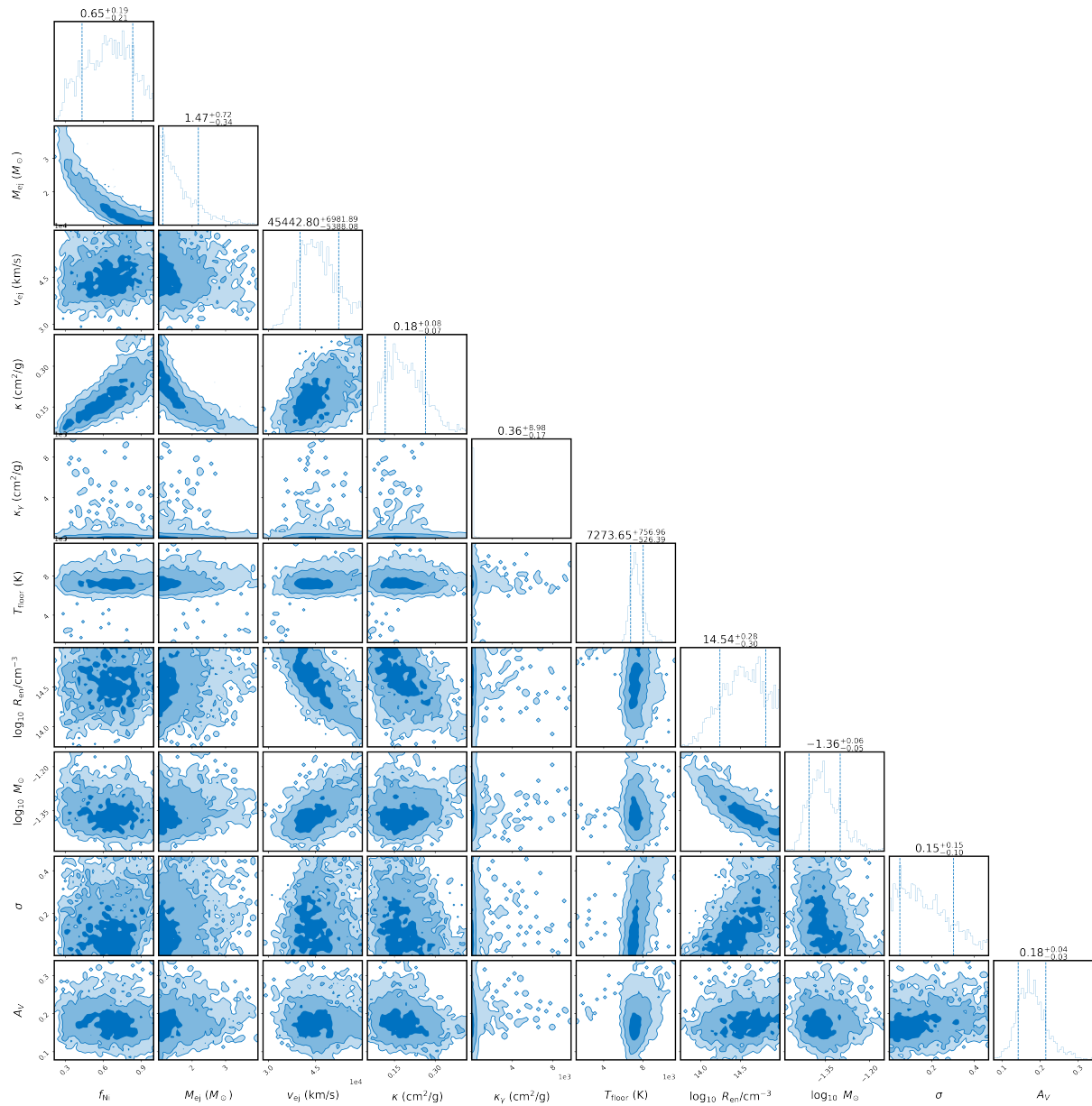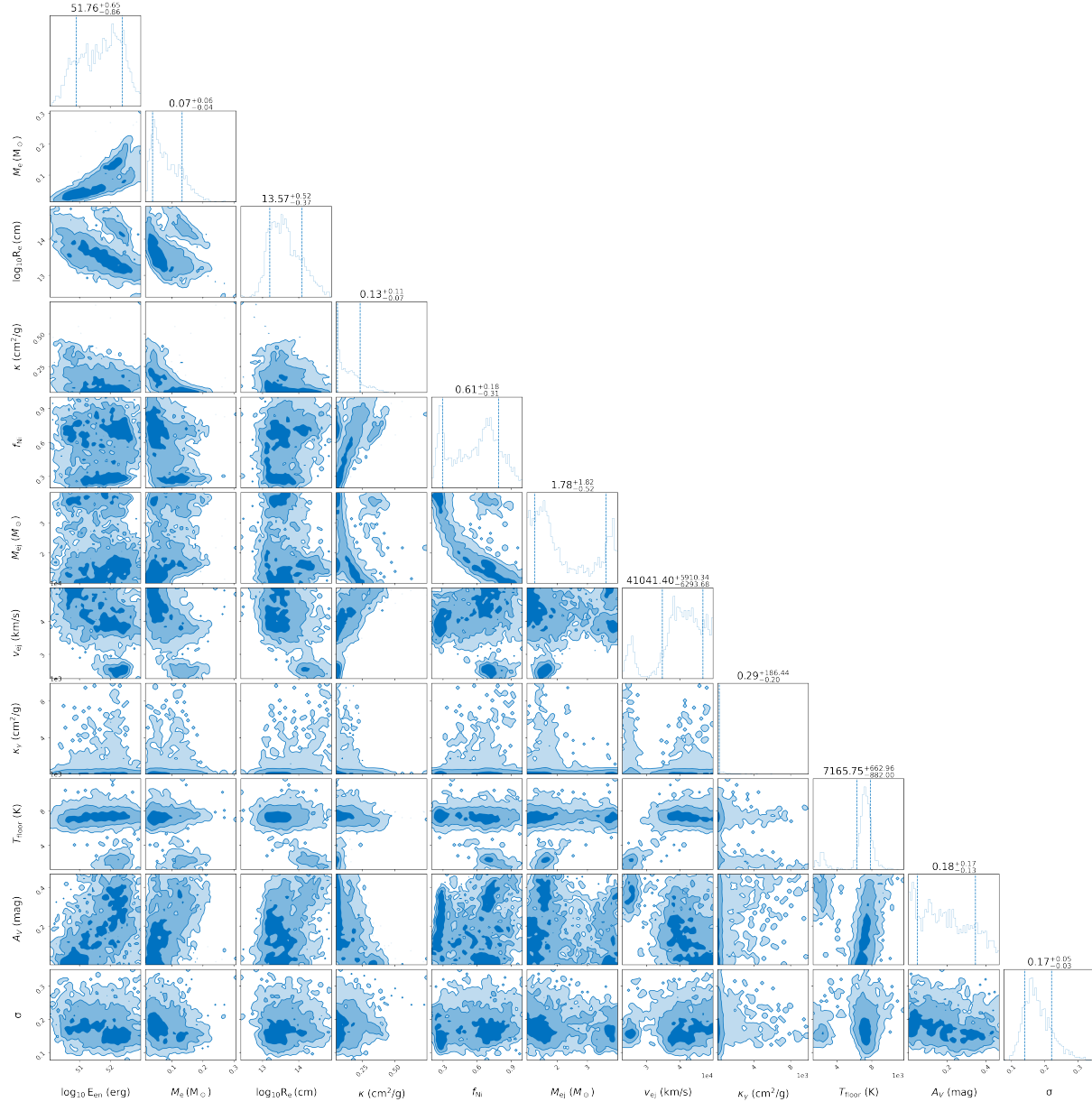
Figure 13. Corner plots associated with fitting the combined SCE model from A. L. Piro et al. (2021) and the radioactive decay model from W. D. Arnett (1982) to the photometry.
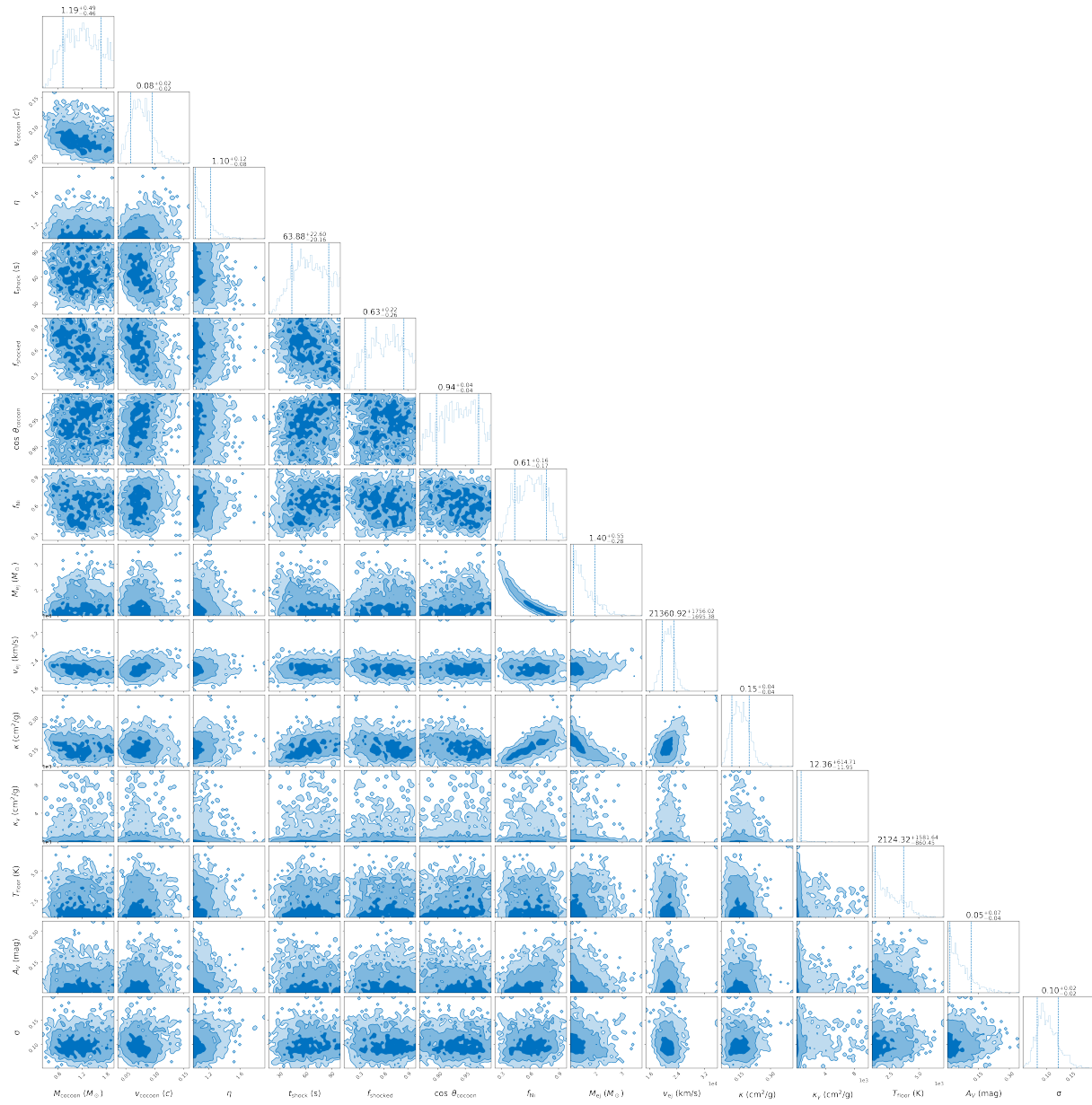
Figure 14. Corner plots associated with fitting the combined shocked cocoon model from E. Nakar & T. Piran (2017) and the radioactive decay model from W. D. Arnett (1982) to the photometry.

Figure 15. Corner plots associated with fitting the combined shocked cocoon model in an extended CSM from E. Nakar (2015) and the radioactive decay model from W. D. Arnett (1982) to the photometry.

Table 8
Spectroscopic Observations of EP250108a/SN 2025kg

$t - T_0$	Tel.+Instr.	Exp. Time (s)	Wavelength Range (Å)
4.6	Gemini+GMOS-South	4×600	3800–7500
9.6	SOAR+GHTS	6×600	3800–7040
14.6	SOAR+GHTS	6×600	3800–7040
14.6	Gemini+GMOS-South	4×600	3800–7500
17.7	Keck+LRIS	3×900	3000–9300
20.6	Gemini+GMOS-South	4×420	3800–7500
25.6	MMT+Binospec	3×900	3900–9240

Note. Epochs are given in observer times since T_0.

Table 9
Optical Photometry and 1σ Errors of EP250108a/SN 2025kg

$t - T_0$	Telescope	Filter	AB Mag	Uncertainty
0.97	Memphisto (X. Zou et al. 2025)	g	20.05	0.14
0.97	Memphisto (X. Zou et al. 2025)	r	20.45	0.17
1.31	LT (R. Eyles-Ferris 2025b)	g	20.10	0.06
1.40	LT (A. Kumar et al. 2025)	g	20.20	0.10
1.40	NOT (Z. P. Zhu et al. 2025b)	r	20.05	0.03
3.21	SAO (A. S. Moskvitin et al. 2025)	r	20.56	0.27
3.35	LT	g	20.53	0.16
3.35	LCO (L. Izzo 2025)	g	20.48	0.10
3.35	LCO (L. Izzo 2025)	r	20.61	0.11
3.36	LT	r	20.64	0.22
3.37	LT	i	20.81	0.25
5.41	LT	g	20.55	0.23
5.42	LT	r	20.64	0.19
5.43	LT	i	20.9	0.17
6.32	LT	g	20.85	0.13
6.34	LT	r	20.65	0.1
6.35	LT	i	20.84	0.11
7.33	LT	g	20.99	0.07
7.34	LT	r	20.6	0.06
7.36	LT	i	20.76	0.08
9.32	LT	g	20.91	0.06
9.33	LT	r	20.33	0.07
14.63	SOAR	g	20.65	0.05
14.63	SOAR	r	20.15	0.02
18.35	LT	g	20.59	0.06
18.35	LT	r	20.21	0.06
18.36	LT	i	20.28	0.07
20.35	LT	g	20.82	0.06
20.35	LT	r	20.23	0.05
20.36	LT	i	20.24	0.07
22.54	SOAR	g	20.96	0.01
22.55	SOAR	r	20.34	0.02
27.51	IMACS	g	21.531	0.06
27.51	IMACS	r	20.541	0.06
27.51	IMACS	i	20.507	0.07
41.37	NOT	r	21.644	0.05

Note. All times are in the observer frame, and the magnitudes are not corrected for Galactic extinction. Photometry obtained by GCNs is indicated with citations.

ORCID iDs

Gokul P. Srinivasaragavan ● https://orcid.org/0000-0002-6428-2700
Hamid Hamidani ● https://orcid.org/0000-0003-2866-4522
Genevieve Schroeder ● https://orcid.org/0000-0001-9915-8147
Nikhil Sarin ● https://orcid.org/0000-0003-2700-1030
Anna Y. Q. Ho ● https://orcid.org/0000-0002-9017-3567
Anthony L. Piro ● https://orcid.org/0000-0001-6806-0673
S. Bradley Cenko ● https://orcid.org/0000-0003-1673-970X
Shreya Anand ● https://orcid.org/0000-0003-3768-7515
Jesper Sollerman ● https://orcid.org/0000-0003-1546-6615
Daniel A. Perley ● https://orcid.org/0000-0001-8472-1996
Keiichi Maeda ● https://orcid.org/0000-0003-2611-7269
Brendan O'Connor ● https://orcid.org/0000-0002-9700-0036
Hanindyo Kuncarayakti ● https://orcid.org/0000-0002-1132-1366
M. Coleman Miller ● https://orcid.org/0000-0002-2666-728X
Tomás Ahumada ● https://orcid.org/0000-0002-2184-6430
Jada L. Vail ● https://orcid.org/0009-0000-4044-8799
Paul Duffell ● https://orcid.org/0000-0001-7626-9629
Ranadeep Dastidar ● https://orcid.org/0009-0000-6548-6177
Igor Andreoni ● https://orcid.org/0000-0002-8977-1498
Aleksandra Bochenek ● https://orcid.org/0009-0008-2714-2507
Seán. J. Brennan ● https://orcid.org/0000-0003-1325-6235
Jonathan Carney ● https://orcid.org/0000-0001-8544-584X
Ping Chen ● https://orcid.org/0000-0003-0853-6427
James Freeburn ● https://orcid.org/0009-0006-7990-0547
Avishay Gal-Yam ● https://orcid.org/0000-0002-3653-5598
Wynn Jacobson-Galán ● https://orcid.org/0000-0003-1103-3409
Mansi M. Kasliwal ● https://orcid.org/0000-0002-5619-4938
Jiaxuan Li (李嘉轩) ● https://orcid.org/0000-0001-9592-4190
Maggie L. Li ● https://orcid.org/0009-0001-6911-9144

References

Anand, S., Barnes, J., Yang, S., et al. 2024, ApJ, 962, 68
Arnett, W. D. 1982, ApJ, 253, 785
Ashton, G., Hübner, M., Lasky, P. D., et al. 2019, ApJS, 241, 27
Balberg, S., & Loeb, A. 2011, MNRAS, 414, 1715
Berger, E., Kulkarni, S. R., Pooley, G., et al. 2003, Natur, 426, 154
Bersten, M. C., Benvenuto, O. G., Nomoto, K., et al. 2012, ApJ, 757, 31
Bertin, E. 2010, SWarp: Resampling and Co-adding FITS Images Together, Astrophysics Source Code Library, ascl:1010.068
Bertin, E. 2013, PSFEx: Point-Spread Function Extractor, Astrophysics Source Code Library, ascl:1301.001
Bertin, E., & Arnouts, S. 1996, A&AS, 117, 393
Bianco, F. B., Modjaz, M., Hicken, M., et al. 2014, ApJS, 213, 19
Blondin, S., & Tonry, J. L. 2007, ApJ, 666, 1024
Bradley, L., Sipőcz, B., Robitaille, T., et al. 2024, astropy/photutils: v2.0.2, Zenodo, doi:10.5281/zenodo.13989456
Brennan, S. J., & Fraser, M. 2022, A&A, 667, A62
Bromberg, O., Nakar, E., Piran, T., & Sari, R. 2011, ApJ, 740, 100
Brown, P. J., Breeveld, A. A., Holland, S., Kuin, P., & Pritchard, T. 2014, Ap&SS, 354, 89
Burrows, D. N., Hill, J. E., Nousek, J. A., et al. 2005, SSRv, 120, 165
Busmann, M., O'Connor, B., Sommer, J., et al. 2025, arXiv:2503.14588
Campana, S., Mangano, V., Blustin, A. J., et al. 2006, Natur, 442, 1008
Cano, Z., Wang, S.-Q., Dai, Z.-G., & Wu, X.-F. 2017, AdAst, 2017, 8929054
Cardelli, J. A., Clayton, G. C., & Mathis, J. S. 1989, ApJ, 345, 245
Cenko, S. B., Frail, D. A., Harrison, F. A., et al. 2010, ApJ, 711, 641
Cenko, S. B., Frail, D. A., Harrison, F. A., et al. 2011, ApJ, 732, 29
Chambers, K. C., Magnier, E. A., Metcalfe, N., et al. 2016, arXiv:1612.05560
Chandra, P., & Frail, D. A. 2012, ApJ, 746, 156
Chevalier, R. A. 1992, ApJ, 394, 599
Chevalier, R. A. 2012, ApJL, 752, L2
Clemens, J. C., Crain, J. A., & Anderson, R. 2004, Proc. SPIE, 5492, 331
Clocchiatti, A., & Wheeler, J. C. 1997, ApJ, 491, 375
Colgate, S. A. 1974, ApJ, 187, 333
Corsi, A., Gal-Yam, A., Kulkarni, S. R., et al. 2016, ApJ, 830, 42
Corsi, A., Ho, A. Y. Q., Cenko, S. B., et al. 2023, ApJ, 953, 179
Das, K. K., Kasliwal, M. M., Sollerman, J., et al. 2024, ApJ, 972, 91
Dastidar, R. G., & Duffell, P. C. 2024, ApJ, 976, 252
Dermer, C. D., Chiang, J., & Böttcher, M. 1999, ApJ, 513, 656
Dey, A., Schlegel, D. J., Lang, D., et al. 2019, AJ, 157, 168
Dressler, A., Bigelow, B., Hare, T., et al. 2011, PASP, 123, 288
Drout, M. R., Chornock, R., Soderberg, A. M., et al. 2014, ApJ, 794, 23
Duffell, P. C., & Ho, A. Y. Q. 2020, ApJ, 900, 193
Eichler, D., & Levinson, A. 1999, ApJL, 521, L117
Eisenberg, M., Gottlieb, O., & Nakar, E. 2022, MNRAS, 517, 582
Eyles-Ferris, R. 2025a, TNSTR, 2025-151
Eyles-Ferris, R. 2025b, GCN, 38878, 1
Eyles-Ferris, R. A. J., Jonker, P. G., Levan, A. J., et al. 2025, ApJL, 988, L14
Fabricant, D., Fata, R., Epps, H., et al. 2019, PASP, 131, 075004
Falk, S. W., & Arnett, W. D. 1977, ApJS, 33, 515
Ferrero, P., Kann, D. A., Zeh, A., et al. 2006, A&A, 457, 857
Foley, R. J., Smith, N., Ganeshalingam, M., et al. 2007, ApJL, 657, L105
Fryer, C. L., Burns, E., Ho, A. Y. Q., et al. 2025, ApJ, 986, 185

Fuller, J. 2017, MNRAS, 470, 1642
Galama, T. J., Vreeswijk, P. M., van Paradijs, J., et al. 1998, Natur, 395, 670
Gehrels, N., Chincarini, G., Giommi, P., et al. 2004, ApJ, 611, 1005
Gianfagna, G., Piro, L., Bruni, G., et al. 2025, arXiv:2505.05444
Gillanders, J. H., Rhodes, L., Srivastav, S., et al. 2024, ApJL, 969, L14
Gimeno, G., Roth, K., Chiboucas, K., et al. 2016, Proc. SPIE, 9908, 99082S
Gompertz, B. P., Fruchter, A. S., & Pe'er, A. 2018, ApJ, 866, 162
Grasberg, E. K., & Nadezhin, D. K. 1976, Ap&SS, 44, 409
Guetta, D., & Della Valle, M. 2007, ApJL, 657, L73
Hamidani, H., & Ioka, K. 2021, MNRAS, 500, 627
Hamidani, H., & Ioka, K. 2023a, MNRAS, 520, 1111
Hamidani, H., & Ioka, K. 2023b, MNRAS, 524, 4841
Hamidani, H., Ioka, K., Kashiyama, K., & Tanaka, M. 2025a, ApJ, 988, 30
Hamidani, H., Sato, Y., Kashiyama, K., et al. 2025b, ApJ, 986, L4
Harrison, R., Gottlieb, O., & Nakar, E. 2018, MNRAS, 477, 2128
Haynie, A., & Piro, A. L. 2021, ApJ, 910, 128
Heise, J., Zand, J. I., Kippen, R. M., & Woods, P. M. 2001, in Gamma-Ray Bursts in the Afterglow Era: Proc. of the Int. Workshop, ed. E. Costa, F. Frontera, & J. Hjorth (Berlin: Springer), 16
Hjorth, J., Sollerman, J., Møller, P., et al. 2003, Natur, 423, 847
Ho, A. Y. Q., Goldstein, D. A., Schulze, S., et al. 2019, ApJ, 887, 169
Ho, A. Y. Q., Kulkarni, S. R., Perley, D. A., et al. 2020, ApJ, 902, 86
Ho, A. Y. Q., Perley, D. A., Gal-Yam, A., et al. 2023, ApJ, 949, 120
Hook, I. M., Jørgensen, I., Allington-Smith, J. R., et al. 2004, PASP, 116, 425
Hu, L., Wang, L., Chen, X., & Yang, J. 2022, ApJ, 936, 157
Hussenot-Desenonges, T., Wouters, T., Guessom, N., et al. 2024, MNRAS, 530, 1
Irwin, C. M., & Hotokezaka, K. 2024, arXiv:2412.06736
Izzo, L. 2025, GCN, 38912, 1
Izzo, L., Auchettl, K., Hjorth, J., et al. 2020, A&A, 639, L11
Izzo, L., Martin-Carrillo, A., Malesani, D. B., et al. 2025, GCN, 39851, 1
Jiang, S.-Q., Xu, D., van Hoof, A. P. C., et al. 2025, arXiv:2503.04306
Kangas, T., & Fruchter, A. S. 2021, ApJ, 911, 14
Kansky, J., Chilingarian, I., Fabricant, D., et al. 2019, PASP, 131, 075005
Kisaka, S., Ioka, K., & Takami, H. 2015, ApJ, 802, 119
Kouveliotou, C., Woosley, S. E., Patel, S. K., et al. 2004, ApJ, 608, 872
Kulkarni, S. R., Frail, D. A., Wieringa, M. H., et al. 1998, Natur, 395, 663
Kumar, A., Maund, J. R., Sun, N. C., et al. 2025, GCN, 38907, 1
Labrie, K., Simpson, C., Cardenes, R., et al. 2023, RNAAS, 7, 214
Lang, D., Hogg, D. W., Mierle, K., Blanton, M., & Roweis, S. 2010, AJ, 139, 1782
Leung, S.-C., Fuller, J., & Nomoto, K. 2021, ApJ, 915, 80
Levan, A. J., Cotter, L., Malesani, D. B., Martin-Carrillo, A., & Jonker, P. G. 2025a, GCN, 38909, 1
Levan, A. J., Rastinejad, J. C., Malesani, D. B., et al. 2025b, GCN, 38987, 1
Li, R. Z., Chen, X. L., Chatterjee, K., et al. 2025a, GCN, 38861, 1
Li, R. Z., Chen, X. L., Chatterjee, K., et al. 2025b, GCN, 38888, 1
Li, W., Leaman, J., Chornock, R., et al. 2011, MNRAS, 412, 1441
Li, W. X., Zhu, Z. P., Zou, X. Z., et al. 2025c, arXiv:2504.17034
Liang, E., Zhang, B., Virgili, F., & Dai, Z. G. 2007, ApJ, 662, 1111
Lin, D., Irwin, J. A., Berger, E., & Nguyen, R. 2022, ApJ, 927, 211
Liu, Y., Sun, H., Xu, D., et al. 2025, NatAs, 9, 564
Liu, Y.-Q., Modjaz, M., Bianco, F. B., & Graur, O. 2016, ApJ, 827, 90
Lyman, J. D., Bersier, D., & James, P. A. 2014, MNRAS, 437, 3848
Lyman, J. D., Bersier, D., James, P. A., et al. 2016, MNRAS, 457, 328
Maeda, K., Suzuki, A., & Izzo, L. 2023, MNRAS, 522, 2267
Margalit, B. 2022, ApJ, 933, 238
Margutti, R., Guidorzi, C., Lazzati, D., et al. 2015, ApJ, 805, 159
Margutti, R., Metzger, B. D., Chornock, R., et al. 2019, ApJ, 872, 18
Matsuoka, M., Kawasaki, K., Ueno, S., et al. 2009, PASJ, 61, 999
Matzner, C. D. 2003, MNRAS, 345, 575
Mazzali, P. A., Deng, J., Maeda, K., et al. 2002, ApJL, 572, L61
Mazzali, P. A., Deng, J., Nomoto, K., et al. 2006, Natur, 442, 1018
McMullin, J. P., Waters, B., Schiebel, D., Young, W., & Golap, K. 2007, in ASP Conf. Ser. 376, Astronomical Data Analysis Software and Systems XVI, ed. R. A. Shaw, F. Hill, & D. J. Bell (San Francisco, CA: ASP), 127
Meegan, C., Lichti, G., Bhat, P. N., et al. 2009, ApJ, 702, 791
Mészáros, P., Rees, M. J., & Wijers, R. A. M. J. 1998, ApJ, 499, 301
Mirabal, N., Halpern, J. P., An, D., Thorstensen, J. R., & Terndrup, D. M. 2006, ApJL, 643, L99
Modjaz, M., Liu, Y. Q., Bianco, F. B., & Graur, O. 2016, ApJ, 832, 108
Modjaz, M., Stanek, K. Z., Garnavich, P. M., et al. 2006, ApJL, 645, L21
Moskvitin, A. S., Spiridonova, O. I. & GRB follow-up Team 2025, GCN, 38925, 1
Nakar, E. 2015, ApJ, 807, 172

Nakar, E., & Piran, T. 2017, ApJ, 834, 28
Nakar, E., Piran, T., & Granot, J. 2002, ApJ, 579, 699
Nakar, E., & Piro, A. L. 2014, ApJ, 788, 193
Nakar, E., & Sari, R. 2010, ApJ, 725, 904
Negoro, H., Kohama, M., Serino, M., et al. 2016, PASJ, 68, S1
Nugent, P., Phillips, M., Baron, E., Branch, D., & Hauschildt, P. 1995, ApJL, 455, L147
O'Connor, B., Pasham, D., Andreoni, I., et al. 2025, ApJL, 979, L30
Oke, J. B., Cohen, J. G., Carr, M., et al. 1995, PASP, 107, 375
Panaitescu, A., & Kumar, P. 2002, ApJ, 571, 779
Pastorello, A., Quimby, R. M., Smartt, S. J., et al. 2008, MNRAS, 389, 131
Pastorello, A., Smartt, S. J., Mattila, S., et al. 2007, Natur, 447, 829
Pélangeon, A., Atteia, J. L., Nakagawa, Y. E., et al. 2008, A&A, 491, 157
Pellegrino, C., Modjaz, M., Takei, Y., et al. 2024, ApJ, 977, 2
Perley, D. A. 2019, PASP, 131, 084503
Perley, D. A., Mazzali, P. A., Yan, L., et al. 2019, MNRAS, 484, 1031
Pian, E., Mazzali, P. A., Masetti, N., et al. 2006, Natur, 442, 1011
Piran, T. 2004, RvMP, 76, 1143
Piro, A. L., Chang, P., & Weinberg, N. N. 2010, ApJ, 708, 598
Piro, A. L., Haynie, A., & Yao, Y. 2021, ApJ, 909, 209
Piro, A. L., & Kollmeier, J. A. 2018, ApJ, 855, 103
Planck Collaboration, Aghanim, N., Akrami, Y., et al. 2020, A&A, 641, A6
Poznanski, D., Ganeshalingam, M., Silverman, J. M., & Filippenko, A. V. 2011, MNRAS, 415, L81
Prentice, S. J., Maguire, K., Smartt, S. J., et al. 2018, ApJL, 865, L3
Pritchard, T. A., Bensch, K., Modjaz, M., et al. 2021, ApJ, 915, 121
Prochaska, J. X., Hennawi, J., Cooke, R., et al. 2020a, pypeit/PypeIt: Release v1.0.0, Zenodo, doi:10.5281/zenodo.3743493
Prochaska, J. X., Hennawi, J. F., Westfall, K. B., et al. 2020b, JOSS, 5, 2308
Pursiainen, M., Childress, M., Smith, M., et al. 2018, MNRAS, 481, 894
Quataert, E., & Shiode, J. 2012, MNRAS, 423, L92
Quirola-Vásquez, J., Bauer, F. E., Jonker, P. G., et al. 2022, A&A, 663, A168
Quirola-Vásquez, J., Bauer, F. E., Jonker, P. G., et al. 2024, A&A, 683, A243
Rabinak, I., & Waxman, E. 2011, ApJ, 728, 63
Rastinejad, J. C., Levan, A. J., Jonker, P. G., et al. 2025, ApJL, 988, L13
Ravasio, M. E., Burns, E., Jonker, P. G. & Fermi-GBM Team 2025a, GCN, 39600, 1
Ravasio, M. E., Burns, E., Wilson-Hodge, C., Jonker, P. G. & Fermi-GBM Team 2025b, GCN, 39146, 1
Rho, J., Evans, A., Geballe, T. R., et al. 2021, ApJ, 908, 232
Rhoads, J. E. 1997, ApJL, 487, L1
Ricci, R., Troja, E., Yang, Y.-H., et al. 2025, ApJL, 979, L28
Rivera Sandoval, L. E., Maccarone, T. J., Corsi, A., et al. 2018, MNRAS, 480, L146
Rodríguez, Ó., Maoz, D., & Nakar, E. 2023, ApJ, 955, 71
Ryan, G., van Eerten, H., MacFadyen, A., & Zhang, B.-B. 2015, ApJ, 799, 3
Sakamoto, T., Lamb, D. Q., Kawai, N., et al. 2005, ApJ, 629, 311
Sapir, N., & Waxman, E. 2017, ApJ, 838, 130
Sarin, N., Ashton, G., Lasky, P. D., et al. 2021, arXiv:2105.10108
Sarin, N., Hübner, M., Omand, C. M. B., et al. 2024, MNRAS, 531, 1203
Schlafly, E. F., & Finkbeiner, D. P. 2011, ApJ, 737, 103
Schmidt, M. 2001, ApJ, 552, 36
Schroeder, G., Ho, A., & Perley, D. 2025, GCN, 38970, 1
Schroeder, G., Laskar, T., Fong, W.-f., et al. 2022, ApJ, 940, 53
Schulze, S., Klose, S., Björnsson, G., et al. 2011, A&A, 526, A23
Shivvers, I., Modjaz, M., Zheng, W., et al. 2017, PASP, 129, 054201
Soderberg, A. M., Kulkarni, S. R., Berger, E., et al. 2004, ApJ, 606, 994
Soderberg, A. M., Nakar, E., Berger, E., & Kulkarni, S. R. 2006, ApJ, 638, 930
Sollerman, J., Jaunsen, A. O., Fynbo, J. P. U., et al. 2006, A&A, 454, 503
Sollerman, J., Kozma, C., Fransson, C., et al. 2000, ApJL, 537, L127
Speagle, J. S. 2020, MNRAS, 493, 3132
Srinivasaragavan, G. P., Swain, V., O'Connor, B., et al. 2024b, ApJL, 960, L18
Srinivasaragavan, G. P., Yang, S., Anand, S., et al. 2024a, ApJ, 976, 71
Srivastav, S., Chen, T. W., Gillanders, J. H., et al. 2025, ApJL, 978, L21
Steele, I. A., Smith, R. J., Rees, P. C., et al. 2004, Proc. SPIE, 5489, 679
Stritzinger, M. D., Taddia, F., Burns, C. R., et al. 2018, A&A, 609, A135
Sun, H., Li, W. X., Liu, L. D., et al. 2025, NatAs, Advanced Online Publication
Sun, H., Zhang, B., & Li, Z. 2015, ApJ, 812, 33
Suzuki, A., Irwin, C. M., & Maeda, K. 2024, PASJ, 76, 863
Suzuki, A., & Maeda, K. 2022, ApJ, 925, 148
Taddia, F., Sollerman, J., Fremling, C., et al. 2019, A&A, 621, A71
Tonry, J. L., Denneau, L., Flewelling, H., et al. 2018, ApJ, 867, 105
Urata, Y., Huang, K., Yamazaki, R., & Sakamoto, T. 2015, ApJ, 806, 222

Valenti, S., Benetti, S., Cappellaro, E., et al. 2008, MNRAS, 383, 1485
van Dalen, J. N. D., Levan, A. J., Jonker, P. G., et al. 2025, ApJL, 982, L47
van Eerten, H., Zhang, W., & MacFadyen, A. 2010, ApJ, 722, 235
Virgili, F. J., Liang, E.-W., & Zhang, B. 2009, MNRAS, 392, 91
Waxman, E., & Katz, B. 2017, in Handbook of Supernovae, ed. A. W. Alsabti & P. Murdin, 967
Waxman, E., Kulkarni, S. R., & Frail, D. A. 1998, ApJ, 497, 288
Whitesides, L., Lunnan, R., Kasliwal, M. M., et al. 2017, ApJ, 851, 107
Williams, P. K. G., Clavel, M., Newton, E., & Ryzhkov, D. 2017, pwkit: Astronomical Utilities in Python, Astrophysics Source Code Library, ascl:1704.001
Wu, S., & Fuller, J. 2021, ApJ, 906, 3
Wu, G.-L., Yu, Y.-W., Liu, L.-D., et al. 2025, arXiv:2505.12491
Xinwen, S., Lei, Y., Haonan, Y., et al. 2025, arXiv:2505.07665
Yadav, M., Troja, E., Ricci, R., et al. 2025, arXiv:2505.08781

Yamazaki, R., Yonetoku, D., & Nakamura, T. 2003, ApJL, 594, L79
Yaron, O., & Gal-Yam, A. 2012, PASP, 124, 668
Yin, Y.-H. I., Zhang, B.-B., Yang, J., et al. 2024, ApJL, 975, L27
Yost, S. A., Harrison, F. A., Sari, R., & Frail, D. A. 2003, ApJ, 597, 459
Yuan, W., Dai, L., Feng, H., et al. 2025, SCPMA, 68, 239501
Yuan, W., Zhang, C., Chen, Y., & Ling, Z. 2022, in Handbook of X-Ray and Gamma-Ray Astrophysics, ed. C. Bambi & A. Sangangelo (Berlin: Springer), 86
Yuan, W., Zhang, C., Feng, H., et al. 2015, arXiv:1506.07735
Yuan, W., Zhang, C., Ling, Z., et al. 2018, Proc. SPIE, 10699, 1069925
Zhang, W., Yuan, W., Ling, Z., et al. 2025, SCPMA, 68, 219511
Zheng, J.-H., Zhu, J.-P., Lu, W., & Zhang, B. 2025, ApJ, 985, 21
Zhu, Z. P., Corcoran, G., Levan, A. J., et al. 2025a, GCN, 38908, 1
Zhu, Z. P., Liu, X., Fu, S. Y., et al. 2025b, GCN, 38885, 1
Zou, X., Liu, C., Kumar, B., et al. 2025, GCN, 38914, 1